Visualisation and quantification of oil-water core annular flow

D.W.S. Vrijlandt

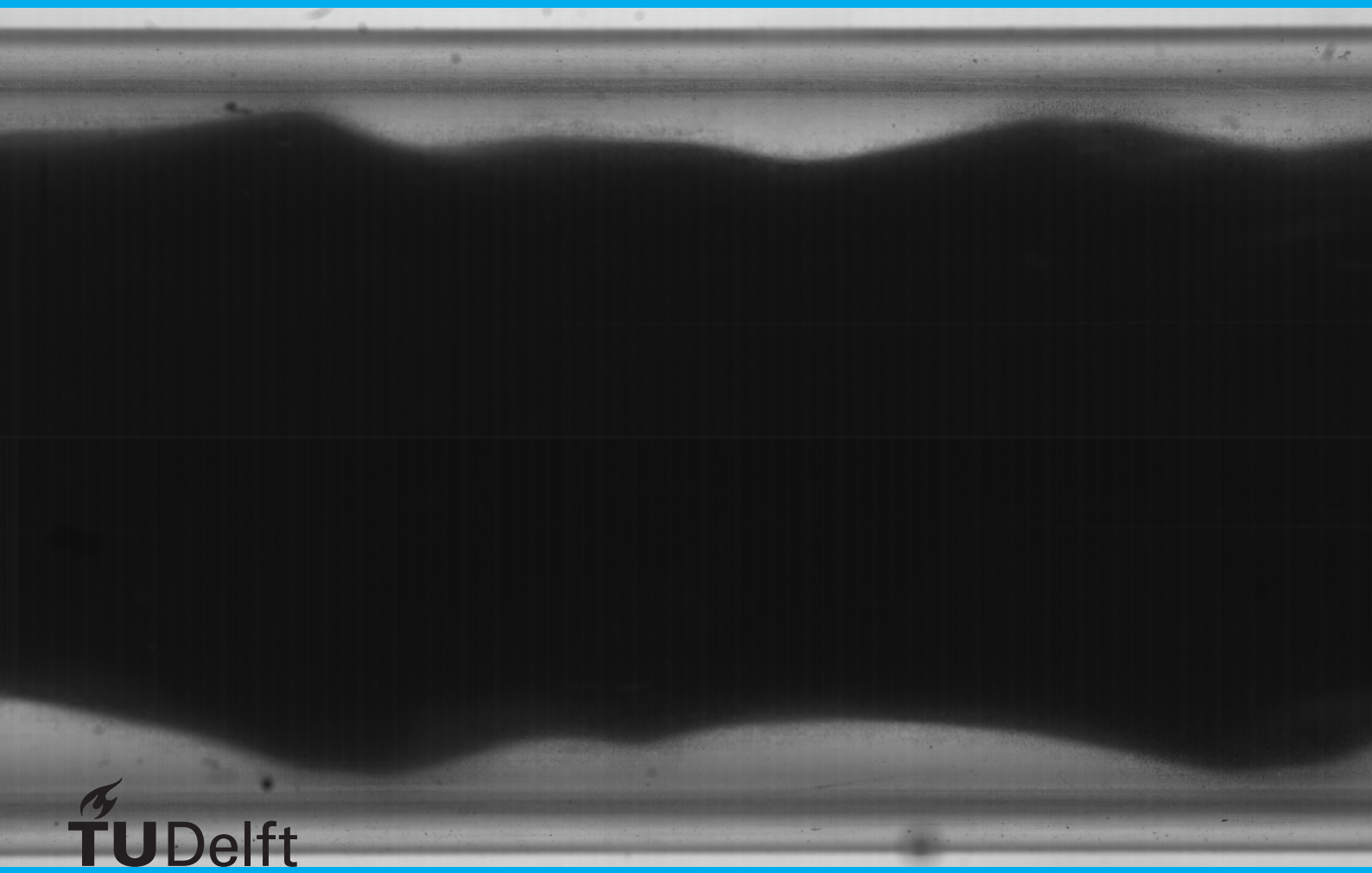

TU Delft

Visualisation and quantification of oil-water core annular flow

by

D.W.S. Vrijlandt

to obtain the degree of Master of Science in Mechanical Engineering
at the Delft University of Technology,
to be defended publicly on 18 December 2020

Student number:	4162951	
Project duration:	1 October, 2019 – 18 December, 2020	
Thesis committee:	Prof. Dr. Ir. R.A.W.M. Henkes	TU Delft, supervisor
	Dr. Ir. M.J.B.M. Pourquie	TU Delft
	Dr. Ir. B.W. van Oudheusden	TU Delft
	Prof. Dr. Ir. G. Ooms	Guest
Report number:	3039	

An electronic version of this thesis is available at `http://repository.tudelft.nl/`.

TU Delft

Abstract

The production of heavy oil from reservoirs requires much more effort than the production of lighter oils. This is due to the fact that this heavy oil has a significantly higher viscosity; namely, typically a factor 10 to 10000 more viscous than water. This higher viscosity makes the transport through pipes less economically viable due to the enormous pressure drop in the pipe. An interesting way to reduce this pressure drop is by creating core annular flow, which is a two phase flow where the less viscous fluid forms an annulus around the viscous fluid. This significantly reduces the pressure drop in comparison to single phase oil flow.

This research focuses on determining the water hold-up in lab experiments of core-annular flow in a horizontal pipe. With the water hold-up and the water cut also the so-called hold-up ratio is known, which is a measure for the oil-water slip. The experiments were conducted for a constant oil flow rate of 0.35 l/s in horizontal pipe with 21 mm diameter. Different water cuts (10 to 20%) and oil/water viscosity ratios (600, 3000) were measured. To determine the water hold-up, the area of the pipe which is occupied by water (or oil) is required. In order to do this the flow is visualised with a high speed camera. Due to the difference in refractive index of the different media that the light has to travel through to eventually reach the lens of the camera, some optical distortion is encountered, which has to be corrected for. The correction procedure was done through a ray tracing analysis which produced a calibration curve that could deduce the actual position of the oil-water interface from the recorded movie. From the temporal and spatial movement of the oil-water interface the waves on this surface were analysed: wave length, wave frequency, wave speed. This was done through applying an autocorrelation function to the interface data. Besides the flow visualisation (to determine the water hold-up and wave characteristics), a pressure transducer was used to measure the pressure drop over a one metre long section of the pipe.

The flow visualisation proved that for low water cuts (10%) the hold-up ratio is significantly higher than that for the higher water cuts (15% and 20%). This means that there is relatively more water accumulation and therefore more oil-water slip when the water cut is reduced. The waves on the interface become longer and the frequency becomes lower with an increasing water cut resulting in an almost constant wave speed. To see the effect of a lower viscosity the temperature of the oil was increased from 20 °C to 40 °C (which decreases the oil-water dynamic viscosity ratio from 3000 to 600). This did not have a noticeable effect on the water hold-up. However, the wave length decreased and the frequency increased which still resulted in a similar wave speed. The results from the experiment have been compared to CFD simulations carried out by PhD candidate Haoyu Li. Interestingly the CFD simulation gives a pressure drop which is roughly 30% lower than the values measured during the experiment. The measured water hold-up fraction is 0.257, whereas the CFD simulation gives 0.255; however, the oil/water interface determined by the simulation is not in agreement with the experimentally recorded interface. The wave frequency given by the CFD simulation is half that which is recorded during the experiment, while the wave length given by the CFD simulation is twice that which is recorded during the experiment. These differences between the CFD simulation and the experiment still lead to an almost equal wave speed.

Preface

This research is done to fulfil the requirements for the degree of Master of Science in Mechanical Engineering at Delft University of Technology. For this research, first the work which had previously been done on the flow loop by Erik van Duin was reviewed and from here the idea came to continue with the visualisation and herewith to quantify the water film layer.

Multiphase flow was introduced to me in the course of Dr. W. P. Breugem & Prof. Dr. Ir. R. A. W. M. Henkes and the parts on pipeline transport and the different flow regimes sparked my interest. After completing the rest of my courses this was the field where I wanted to do my thesis in. I would like to thank Prof. Henkes for providing this thesis opportunity, supervision and the helpful discussions. Furthermore I would like to thank Dr. Ir. M.J.B.M. Pourquie and Prof. Dr. Ir. G. Ooms who helped with the discussion and gave me a lot of new insights; their vast experience on this subject has been a great help to me.

I would also like to express my gratitude to everyone who helped me during this project. The technical support staff of the fluid mechanics department: Edwin Overmars, Jasper Ruijgrok & Jan Graafland for their help with the cameras, sensors and calibration pieces which required assembly. The P&E lab supervisors: Jaap van Raamt and Michel van den Brink. PhD candidate Haoyu Li for her help with the MATLAB analysis of the images, the help during a couple of the experiments and providing data from her simulations.

I would also like to thank Audrey for proofreading my thesis a couple of times and make it more readeable. Last but not least I want to thank my family and especially my parents for giving me the opportunity to attend university at TU Delft and enjoy my student time.

D.W.S. Vrijlandt
Rottterdam, December 10, 2020

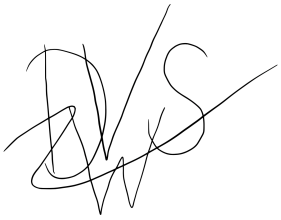

Contents

Nomenclature

Abreviations

CAF	Core annular flow
SD	Standard deviation
PLIF	Planer laser induced fluoresense

Symbols

A	Area	m^2
f	Fanning friction factor	-
R	Radius	m
u	Velocity	$m\,s^{-1}$
v	Phase velocity	$m\,s^{-1}$
$\dot{V}$	Volumetric flow rate	$m^3\,s^{-1}$
γ	Surface tension	$N\,m^{-1}$
μ	Dynamic viscosity	Pa s
ν	Kinematic viscosity	$m\,s^{-1}$ or cSt
ρ	Density	$kg\,m^{-3}$
σ	Surface tension coefficient	$N\,m^{-1}$
τ	Shear stress	Pa

Subscripts

d	Drag
e	Spherical equivalent
in	Inner
j,s	superficial velocity of phase j
o	Oil
out	Outer
t	Terminal
w	Water

List of Figures

List of Tables

1

Introduction

As the oil demand is still increasing (figure1.1 [18]), and the need to utilise heavy oil wells is also increasing. Previously, these kind of oil reserves were not interesting due to the fact that light oil was still available in large amounts. However to utilise these heavy-oil reservoirs in an economically viable way and to be able to meet volume demands, a new way of transporting oil through pipes is required. A way to achieve this could be the efficient use of two phase liquid-liquid flow mechanics. This chapter introduces the concept of two phase liquid-liquid flow and will explain the research purpose and the layout of this report.

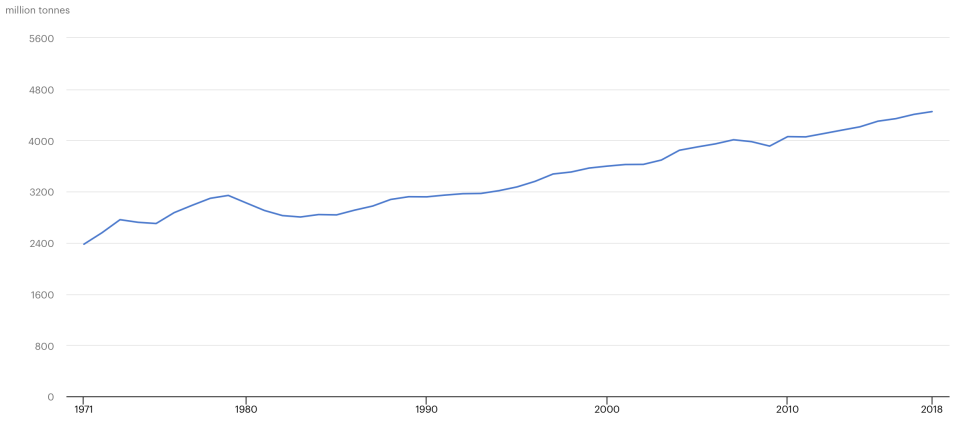

Figure 1.1: World oil demand, 1971-2018

1.1. Multiphase flow

Multiphase flow is the simultaneous flow of two or more immiscible fluids. This can be two different thermodynamic phases but it can also be two different liquids which are immiscible. The two phase flow of interest in this research is oil-water flow which has a density ratio close to unity and a large viscosity ratio.

Within liquid-liquid flow, nature has a strong tendency to order them in such a way that the least viscous fluid is in the region of high shear (with a high value for $\frac{\partial u}{\partial y}$) [21]. The fluids can rearrange themselves in several different ways depending on their fluid properties and velocities; the different flow patterns are displayed in figure 1.2. The pattern of interest for this research is the flow pattern shown in figure 1.2 (annular flow) which can only be achieved when there is a significant viscosity difference between the fluids. This flow pattern is called core annular flow, from now on referred to as CAF .

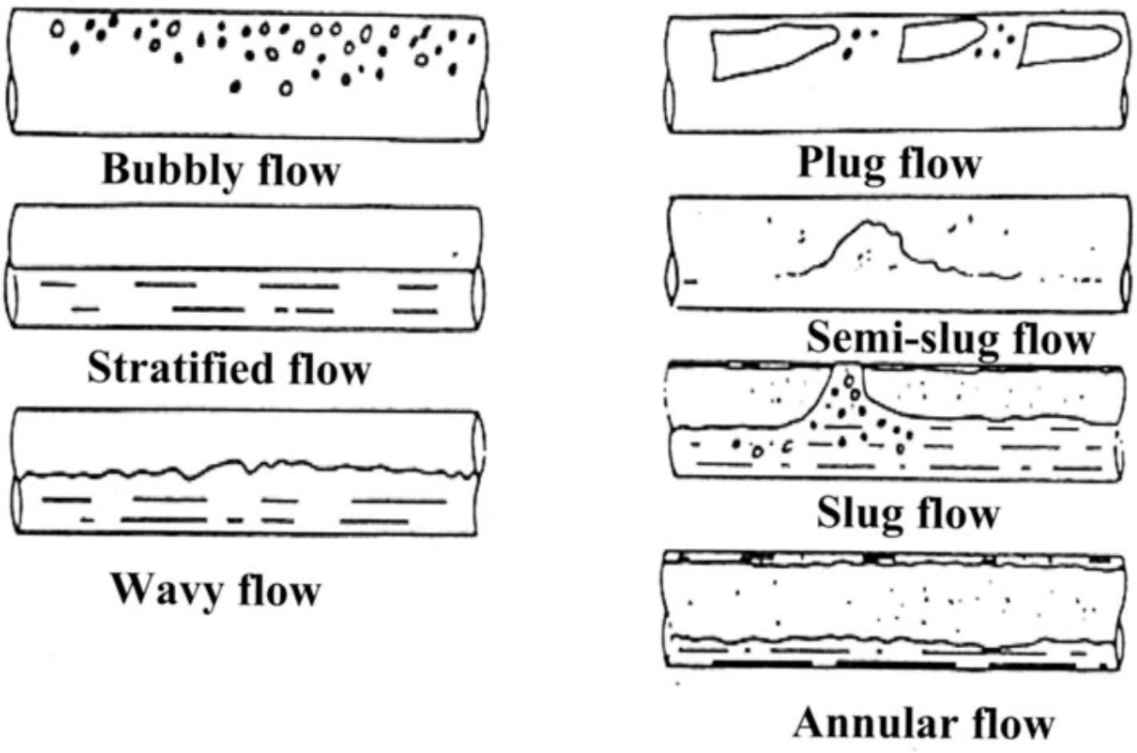

Figure 1.2: The different flow patterns in horizontal multiphase flow adapted from Azzopardi 2003[4]

CAF has been studied a lot throughout the years, as it has interesting industrial applications. It can be used for the transport of highly viscous fluids such as certain oils. The water present in CAF acts as a lubricant for the viscous oil core. This significantly lowers the pressure drop compared to single phase oil flow.

1.2. Research purpose

As discussed in the previous section, core annular flow is interesting for transporting highly viscous fluids. To apply this on an industrial scale, however, more research is needed and the phenomenon must be understood better.

This project focuses on getting quantitative measurements of the water film thickness for the flow in a horizontal pipe. This to eventually be able to determine the water hold-up and the interfacial wave characteristics. This will be done through images recorded from the experimental setup.

1.3. Report outline

Chapter 2 will give background information on CAF. In chapter 3 the experimental set up which was used during this research will be described and explained. Chapter 4 will discuss the calibration procedures used for the pressure transducer and show the correction procedure for the optical distortion encountered due to the circular geometry of the tube. In chapter 5 the different procedures necessary to get the data required for this research are described. The results of this research will be given in chapter 6 followed by the conclusion and recommendations of this research in chapter 7.

2

Theoretical background

In this chapter the theory behind the liquid-liquid two phase flow will be elaborated. To begin, the important parameters which influence the flow will be introduced. Next the concept of optical distortion will be introduced and explained. To conclude this chapter relevant research done on film measurements in horizontal oil-water pipe flow will be shown.

2.1. Liquid-liquid two phase flow

There are several flow patterns associated with liquid-liquid flow (see Chapter 1). These flow patterns depend on three parameters: pipe characteristics, flow velocities and fluid properties. The pipe characteristics are defined by the diameter and wall roughness. The fluid properties are defined by the fluid density, viscosity and surface tension. This density difference has a significant effect on the eccentricity of the flow. In liquid-liquid systems, however, the density is usually close to unity but the viscosity difference can be significant. In the experiment under investigation the viscosity ratio is 3000 and 600.

2.1.1. Pipe characteristics

The pipe characteristics are defined by the diameter which relates to the area and the wall roughness. The wall roughness of the PMMA pipe is taken to be a constant: $k_{\mathrm{PMMA}} = 0.015$ mm [14]. The diameter of the pipe is defined as: $D_{\mathrm{in}} = 2r_{\mathrm{in}}$ where r_{in} is the inner radius of the pipe. A schematic of the pipe is given in figure 2.1.

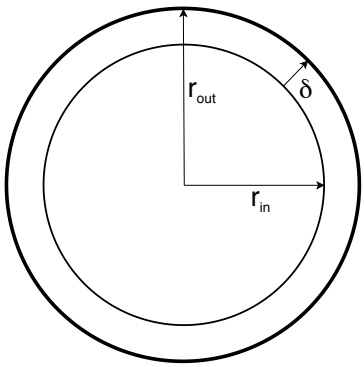

Figure 2.1: Schematic of the pipe dimensions

For the optical distortion the refractive index and thickness of the tube wall are of interest. These are defined as $n_{\mathrm{PMMA}} = 1.491$ (adapted from the technical data sheet provided by the producer see appendix A) and the thickness of the pipe wall, which is $\delta = 2$ mm.

2.1.2. Flow velocities

In single phase flow the flow velocity is defined as the volumetric flow rate divided by the cross-sectional area of the pipe. In multiphase flow there is more than one volumetric flow rate so the parameter superficial velocity is introduced. This superficial velocity can be described as the velocity if there was only a single phase present:

$$u_{s,j} = \frac{\dot{V}_j}{A} \tag{2.1}$$

In this equation j denotes the phase of interest, A is the cross-sectional area of the pipe and $\dot{V}_j$ is the volumetric flow rate. If the superficial velocities are summed the mixture velocity is obtained, which can be expressed as:

$$u_{\text{mix}} = \frac{\dot{V}_1 + ... + \dot{V}_n}{A} \tag{2.2}$$

2.1.3. Fluid properties

During this experiment tap water was used with its coresponding values [13, 15, 16]. The oil used in this experiment is Shell Morlina S4 680. The properties of this oil are provided by the vendor (see appendix B). Measurements were carried out to validate these properties see table 2.1

Table 2.1: Fluid properties of water at $15°$C & Oil at $20°$C

Property	Symbol	Water	Oil	Unit
Density	ρ	999.06	913.1	kg m^{-3}
Dynamic Viscosity	μ	$1.1373 * 10^{-3}$	3.048	N s m^{-2}
Kinematic Viscosity	ν	1.1384	3339	cSt
Surface tension	γ	72.02	13.8	mN m^{-1}

Oil dynamic viscosity

To measure the viscosity of the oil, a MCR 302 rheometer from Anton Paar was available for use at the waterlab of the TU Delft. The rheometer is used to see how a liquid reacts on an applied force. The rheometer used for this experiment is a shear rheometer. It uses a Taylor-Couette flow geometry by rotating the centre piece while keeping the wall of the cup stationary. By applying different shear rates the viscosity of the oil can be determined as a function of the shear rate. The results of these measurement are shown in figure 2.2. Since the viscosity of the oil at different temperatures is of interest, the oil is put into a cup that is placed in the rheometer. This cup is heated by a thermal bath surrounding it.

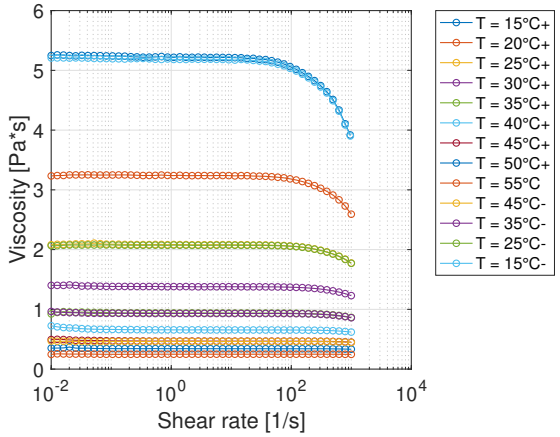

Figure 2.2: Results of the rheometer measurements

The + values correspond to the oil being heated from 15 to 55 °C and the - values correspond to the oil temperature going down from 55 to 15 °C. From these measured values a curve fit can be acquired leading to the following formula for the oil viscosity as a function of temperature:

$$\mu(T) = 20.71exp(-0.1216T) + 4.034exp(-0.05256T) \tag{2.3}$$

Where T is the temperature in degrees Celsius and μ is the dynamic viscosity in Pascal second.

Oil density

For the density measurement a DMA 5000 digital density meter from Anton Paar is used, which was readily available in the PE lab. This machine uses a sample of approximately 2ml of oil and measures with an accuracy of six digits.
The results from these measurements are shown in figure 2.3. What becomes clear from this figure is that the density decreases with increasing temperature.

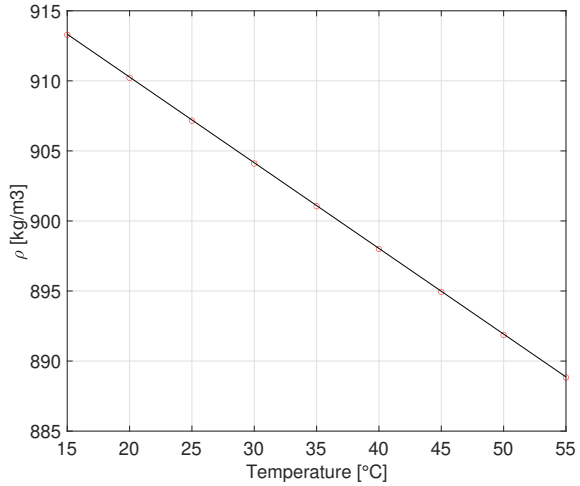

Figure 2.3: Results of the density measurements

Similarly to the viscosity function a density function can be acquired resulting in:

$$\rho(T) = 922.5 - 0.6115T \tag{2.4}$$

Where T is the temperature in degrees Celsius and ρ is the density in kilograms per cubic metre.

Oil kinematic viscosity

After acquiring both these properties the kinematic viscosity can be determined and compared to the vendor's properties. The kinematic viscosity is defined as the dynamic viscosity (μ) divided by the density (ρ) .

$$\nu = \frac{\mu}{\rho} \tag{2.5}$$

The results for the viscosity curve are shown in figure 2.4.

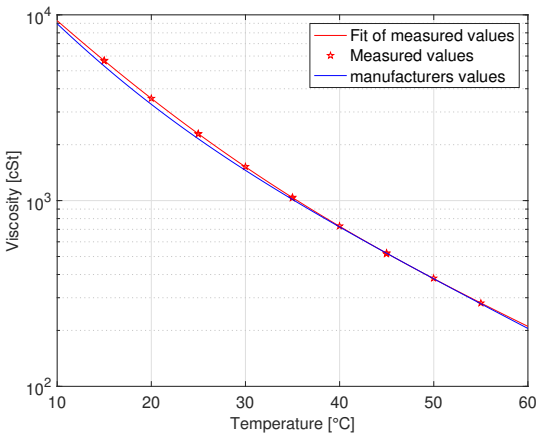

Figure 2.4: Kinematic viscosity: vendors (blue) vs measured (red)

An overview of the important data is given in table 2.2.

Table 2.2: comparison of vendor's properties vs measured

	Measured [cSt]	Vendor [cSt]
Density @15°C	913	910
Kinematic Viscosity @40°C	727	680
Kinematic Viscosity @100°C	-	37

2.1.4. Dimensionless numbers

Dimensionless numbers play an important role when analysing fluid dynamics. The dimensionless numbers of interest for horizontal CAF are displayed in table 2.3.

Table 2.3: Dimensionless numbers and their expressions

Dimensionless number	abbreviation	Definition	Expression
Density ratio	λ	$\frac{\text{Density of fluid 1}}{\text{Density of fluid 2}}$	$\frac{\rho_1}{\rho_2}$
Viscosity ratio	κ	$\frac{\text{Viscosity of fluid 1}}{\text{Viscosity of fluid 2}}$	$\frac{\mu_1}{\mu_2}$
Water cut	WC	$\frac{\text{Volumetric flow rate of water}}{\text{Total volumetric flow rate}}$	$\frac{\dot{V}_w}{\dot{V}_w+\dot{V}_o}$
Hold-up fraction	α_j	$\frac{\text{Area of fluid j}}{\text{Total area}}$	$\frac{A_j}{A}$
Hold-up ratio	H	$\frac{\text{Volumetric flow rate fluid 1/volumetric flow rate fluid 2}}{\text{Area fluid 1/area fluid 2}}$	$\frac{\dot{V}_o/\dot{V}_w}{A_w/A_o}$
Froude number	Fr	$\frac{\text{Inertial forces}}{\text{Gravitational forces}}$	$\frac{\mathcal{U}}{\sqrt{g\mathcal{L}}}$
Eötvös number	Eo	$\frac{\text{Gravitational forces}}{\text{Capilary forces}}$	$\frac{\Delta\rho g\mathcal{L}^2}{\gamma}$
Reynolds number	Re	$\frac{\text{Inertial forces}}{\text{Viscous forces}}$	$\frac{\rho\mathcal{U}\mathcal{L}}{\mu}$

In this table $\mathcal{L}$ and $\mathcal{U}$ are the characteristic length scale and characteristic velocity, respectively. during this research the water cut and hold-up fraction will be of main importance. The water cut is changed during the different experiments and the hold-up fraction is the result of the measurement.

2.2. Levitation mechanism

Due to the density difference a vertical force works on the core of the CAF. This force is the buoyant force. In order to keep horizontal core annular flow stable and to prevent the oil to foul the top pipe wall, this buoyant force has to be counteracted; this is done by the waves that form on the interface between the two phases. These waves account for the hydrodynamic force acting downward on the core. The core is being levitated and the mechanism that keeps the core from touching the inner wall of the pipe is called the levitation mechanism. There are two theories relating to this subject; both will be disused in this section.

2.2.1. Hydrodynamic lubrication theory

The levitation model proposed by Ooms et al. [26] assumes that the core is a solid body simplifying the oil-water interface to a solid-liquid interface. In this model the interface is modelled as a sawtooth-shape which is independent of the tangential coordinate and only depends on the x-coordinate (direction of flow). The movement of this sawtooth-shaped interface through the pipe generates a pressure variation in the water film. This induces a force that is large enough to counteract the buoyancy force. The driving force for this pressure variation is due to viscosity and thus works for low Reynolds numbers where viscosity dominates. A schematic of this flow is shown in figure 2.5

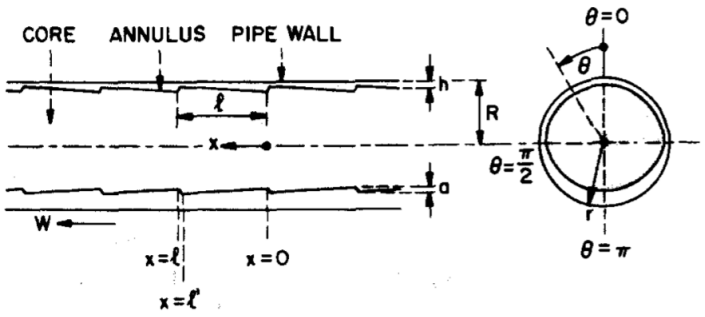

Figure 2.5: Schematic of the model proposed by Ooms et al.[26]

2.2.2. Flying core model

Joseph et al. [21] proposed a model where the driving force is the inertial force. They argue that a lift needs to be generated due to inertia. This lift is described as in Liu's [24] formula for capsule lift-off in a pipeline, concluding that the critical lift of velocity is proportional to the square root of gravity times the density difference as an inertial criterion. This model also accounts for the smoothing due to higher and lower pressure regions which is also discussed in the model of Ooms et al.[26]. A schematic of this flow is shown in figure 2.6.

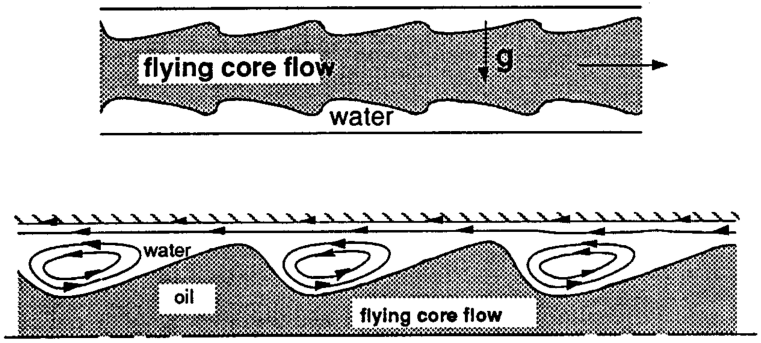

Figure 2.6: Schematic of the model proposed by Joseph et al.[21]

The main difference between the shape of the core between these models is the orientation of the waves; in the flying core the steep part of the wave is directly after the crest, but in the lubrication driven model the steep part of the wave is in front of the crest. Since the flying core model is inertia driven this should be applied for high Reynolds numbers (inertia driven flow) and the lubrication model should be applied for low Reynolds number (viscosity driven flow).

2.3. Pressure drop and hold-up

Experimental research has shown that the pressure drop in core annular flow is almost independent of the oil viscosity and only slightly higher than in single phase water flow at the same mixture velocity. In this research the flow consists of a turbulent annulus of water and a laminar core of oil. There are two, relevant flow correlations for CAF: one proposed by Ullmann and Brauner [31] and another one proposed by Bannwart [5]. From Van Duin's research it became clear that the model of Ullmann and Brauner showed the best agreement with the measurement results and it also predicts the water hold-up that is of interest for this research. This is why only the Ullmann and Brauner model will be tested.

2.3.1. Ullmann and Brauner model for core annular flow

The two fluid-model proposed by Ullmann and Brauner [31] assumes that the flow is fully developed and that the two phases are immiscible. With these assumptions the equations of motion for both phases are constructed. This system of equations contains more unknown variables than equations making the use of closure models necessary. These closure models are used for the interface shear stress and the wall shear stress.

The analysis leads to the following dimensionless numbers, $\mathcal{X}^2$ the Martinelli parameter, c_i, the ratio between the velocity of the interface and the velocity of the annulus, $\widetilde{\alpha}_\mathrm{w}$ is the explicit solution for the in situ hold-up and $\frac{d\widetilde{P}_\mathrm{o}}{dZ}$ is the dimensionless pressure drop.

The Martinelli parameter is an expression for the phase fraction of a flow. For laminar core and turbulent annulus this leads to:

$$\mathcal{X}^2 = \frac{0.046}{16}\left(\frac{\nu_\mathrm{w}}{\nu_\mathrm{o}}\right)^{0.2}\frac{\rho_\mathrm{w}}{\rho_\mathrm{o}}\frac{\mathrm{Re}_{\mathrm{o,s}}^{0.8}}{\widetilde{Q}^{1.8}} \tag{2.6}$$

Where $\mathrm{Re}_{\mathrm{o,s}}$ is the Reynolds number with the superficial oil velocity as characteristic velocity. $\widetilde{Q}$ is defined as the ratio between the superficial velocities of the oil and water phase:

$$\widetilde{Q} = \frac{Q_\mathrm{o}}{Q_\mathrm{w}} = \frac{u_{\mathrm{o,s}}}{u_{\mathrm{w,s}}} \tag{2.7}$$

For a turbulent annular phase the interface slip ratio is assumed to be: $c_\mathrm{i} \simeq 1.15 \div 1.2$.

The in situ water hold-up is approximated as:

$$\widetilde{\alpha}_{water} = \frac{0.5c_\mathrm{i} - \mathcal{X}^2\widetilde{Q} + 0.5c_\mathrm{i}\sqrt{1 + 4\mathcal{X}^2\left(\widetilde{Q}/c_\mathrm{i}\right)}}{c_i + \widetilde{Q} - \mathcal{X}^2\widetilde{Q}} \tag{2.8}$$

Now a relation between the pressure drop of the core annular flow in comparison to single phase oil flow flow can be defined as:

$$\frac{d\widetilde{P}_\mathrm{o}}{dZ} = \frac{\mathcal{X}^2}{\widetilde{\alpha}_{water}^2} \tag{2.9}$$

This is a method to evaluate potential pressure drop reduction in concentric core annular flow.

2.3.2. Empirical water hold-up correlation

Besides the theoretical model provided by Ullmann and Brauner there is also a correlation found by Arney et al. [3] which is based on twelve experiments:

$$H = WC[1 + 0.35(1 - WC)] \tag{2.10}$$

In this equation WC is defined as the water cut that is defined as the volumetric flow rate of water divided by the total volumetric flow rate. H is the hold-up ratio which is defined as the ratio of the flow rates divided by the ratio of the hold-up of the liquids present. Both values are also described in table 2.3. Note that the hold-up fraction can also be expressed as: $H = \alpha_w/\alpha_o * (1 - WC)/WC$. This is also a measured for the apparent slip between the water and oil. If h>1 there is relatively much water accumulation and the water bulk velocity is lower than the oil bulk velocity. When $\alpha_w = WC$ there is no slip between the phases.

2.4. Optical distortion

Due to the circular surface of the pipe the image will be distorted. This optical distortion can lead to significant errors in geometrical measurements (e.g. solid particles, interfaces). This occurs when the light has to pass through several media with different refractive indices.

2.4.1. Snell's law

The refractive index is a dimensionless number which is defined as:

$$n = \frac{c}{v} \tag{2.11}$$

where c is the speed of light and v is the phase velocity in a specific medium. This refractive index is an indication of how much slower the light moves through a specific medium compared to a vacuum. Due to this difference of the speed with which light travels in different media the optical path can be 'bended' slightly when going from one medium to another. This can be described by Snell's law which states:

$$n_1 \sin(\theta_1) = n_2 \sin(\theta_2) \tag{2.12}$$

Where θ_1 is the angle with the normal at the interface from medium 1 to medium 2 and θ_2 is the angle with the normal on the other side of this interface. A schematic of this is shown in figure 2.7(a). In this figure the refractive indices are $n_1 < n_2$, meaning that the velocity is lower in medium 2 than in medium 1 resulting in a smaller angle.

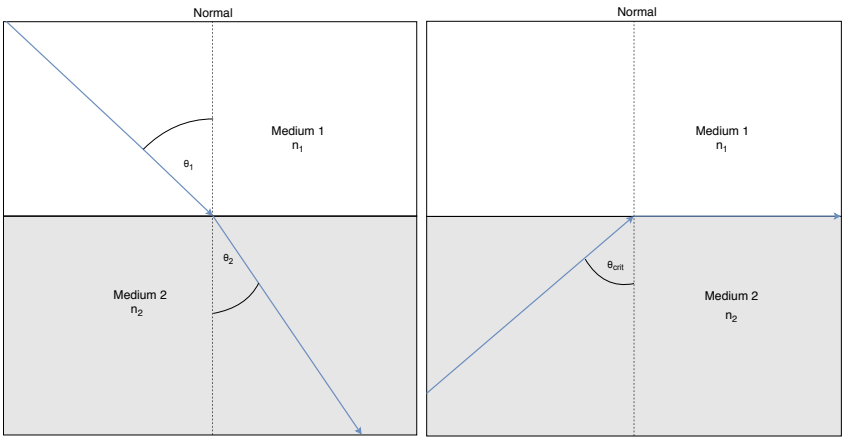

(a) Visualisation of Snell's law ($n_1 > n_2$) (b) Visualisation of the critical angle ($n_1 > n_2$)

Figure 2.7: Visualisation of situations where incoming angle $<$ critical angle and incoming angle $=$ critical angle

If the refraction goes from a medium with a high refractive index to a lower refractive index it is possible that a total internal reflection occurs (shown in figure 2.7(b)). The incoming angle for which this happens is called the critical angle, which can be expressed as:

$$\theta_{crit} = \arcsin\left(\frac{n_2}{n_1}\sin(90°)\right) \tag{2.13}$$

The effect of this refraction in a curved surface creates a lens like effect enlarging the image closer to the wall making it hard to quantify the photos taken by the camera.

2.4.2. Ray tracing analysis

For the ray tracing analysis the light beams going through the pipe are followed from the centre of the pipe to the point where the camera lens is positioned. At every refraction point the angle of incidence is determined from which the outgoing angle is calculated through Snell's law (equation 2.12). Since the inner surface of the pipe is curved, a transformation is needed to find the angle between the incoming angle and the perpendicular of the pipe wall. This perpendicular line is shown as the dashed line in figure 2.7(a). Finding this angle is done by looking at the angle from the centre of the pipe to the point of intersection, displayed as angle α_h in figure 2.8, which is a representation of a refraction happening at a circular interface like the pipe in this experiment.

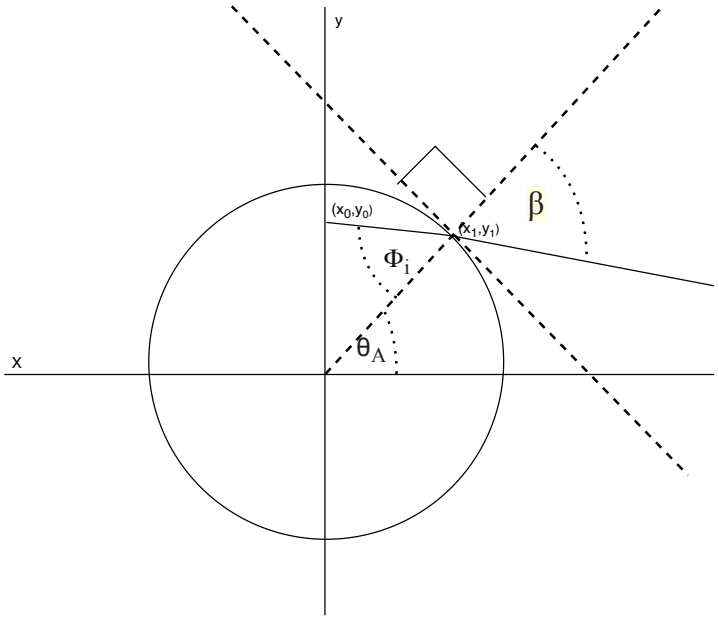

Figure 2.8: A schematic of the incoming ray at the point of refraction

For the calculation of the in- and out-going angles the following equations are derived; note that Φ_i and β describe the incoming- and outgoing-angle in the transformed (x',y') domain and θ_A describes the angle between the origin and the place of intersection of light and inner wall in the normal domain (x,y):

$$\Phi_i = \theta_A - \beta \tag{2.14}$$

Where θ_A is the angle for the location where the ray hits the intersection between two media and the x-axis at point (x_0, y_0):

$$\theta_A = arctan\left(\frac{y_1 - y_0}{x_1 - x_0}\right) \tag{2.15}$$

Herewith the outgoing angle can be calculated in the frame of reference of the point of intersection:

$$\beta = \arcsin\left(\frac{n_1}{n_2}\sin(\alpha_i)\right) \tag{2.16}$$

This can be inverted to the 'normal' frame of reference (x- and y-axes) through:

$$\beta = \theta_A - \beta \tag{2.17}$$

These steps are repeated for the outer wall of the pipe and for the wall of the optical box. At the optical box, however, there is no need for a transformation of the axes due to the fact that the walls of the optical box are perpendicular to the x-axis.
Two important parameters for the ray tracing analysis are:

- Offset (The vertical location of the centre of the camera with respect to the centre of the pipe)
- Pixel size (This is based upon the outer diameter of the pipe which is a known distance)

For every experiment these values are calculated and a different calibration curve will be obtained based upon these values. There is only one variable that influences the shape of the calibration curve, namely the Offset. The sensitivity of the calibration curve will be tested in chapter 4.

After all these actions have been taken the final distortion can be calculated by applying the following formulas:

$$BM = AB\sin(\theta_A - \beta) \tag{2.18}$$

Where,

$$AB = R_0 \frac{\sin(\theta_A - \theta_B)}{\sin(180 - \beta)} \tag{2.19}$$

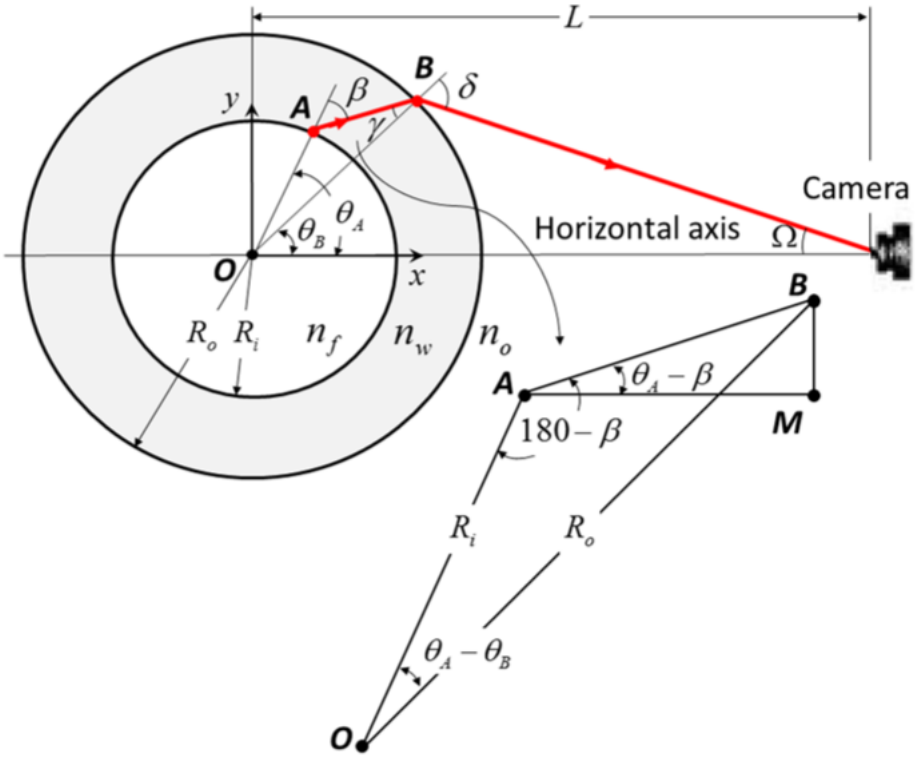

Figure 2.9: Picture to clarify the optical distortion adapted from Drazi et al.[12]

In chapter 3 the results of the ray tracing analysis are discussed, which provides the effect of the different media on the refraction of the light beams. This approach is based on the paper by Darzi et al.[12].

2.5. Experimental research

A lot of research has been done on CAF; both the pressure drop and the film thickness have been measured extensively. In this section the methods which have been used to measure the film thickness will be discussed, after which the pressure drop measurements will be discussed. Concluding with an overview of the different methods with their pros and cons and the reason for using the specific methods in this research.

2.5.1. Film thickness measurement

In previous experimental research many different methods have been used to determine the film thickness of the water annulus. In this section an overview of the different measurement methods and results from previous research is given. A film thickness measurement is also possible with acoustic measurement techniques; however, the wavy interface of the flow present in CAF would prove significant difficulties in detecting the reflected ultrasonic wave.

Electrical methods

Conductance based methods: this technique imposes an electrical potential difference between electrodes and measures the resulting current. There are two different ways of applying this method, it can be done with probes that are flush mounted with the inner pipe wall and the current between the probes is measured. For the other method wires are inserted inside the pipe and the current is measured between these wires. For both methods the conductivity between these probes or wires is related to the amount of water between these detection devices. Research with the probes has been done by Coney (1973) [11] and research with the wires method has been done by Koskie et al. (1989) [23] and more recently by Andreussi et al. (2016) [2].

Capacitance based methods: this technique uses two opposing plates which are submitted to an electrical current. This creates a capacitance with a value that depends on the plate area, the dielectric constant of the media between the plates and the distance between these plates. This method provides the water hold-up fraction and will not give any information about the thickness of the water layer. Capacitance measurements were done by An et al. (2014) [1] and Strazza et al. (2011) [30]. Recently a new technique was applied by Bonilla-Riano et al. (2019) [7]; that technique uses multiple send and receive sensors . With these sensors the capacitance at different positions can be measured; with these values the film height can be determined.

Optical methods

Interface detection: for this technique a movie is recorded of the flow with a high speed camera. The colour gradient between the black oil and transparent water is detected by applying a binarization algorithm to the image with a threshold which makes the core full black and the rest of the image white. The black pixel can be detected and the position of the interface can be determined. During the previous work at the set-up by van Duin (2017)[33] images like these were made, these images have been analysed by Konings (2017) [22].

Planer laser induced fluorescence (PLIF): this techniques requires a dye to be injected in the water. When this dye is subjected to a laser field it will induce fluorescence. This fluorescence has an intensity that depends on the thickness of the water layer, which can thus be used to determine the annulus thickness. This technique was applied for stratified oil-water flow by Morgan et al.(2013) [25] and Ibarra et al. (2016) [17]. It has also been applied to a falling film by Rajamani (2018) [27] and might also be applicable for CAF.

2.5.2. Pressure drop measurement

The pressure drop is measured by taking the pressure difference between two points in the pipe. This pressure difference can either be measured with an inverted U-tube manometer or a differential pressure transducer. Both these methods have previously been used at the current set-up, the inverted U-tube manometer method was applied by Ingen Housz [19] and the differential pressure transducer was used by van Duin [33]. The pressure transducer gives an electrical signal which can be registered in a data acquisition device, where the inverted U-tube manometer has to be manually read and registered, due to this the differential pressure transducer has a clear advantage. The differential pressure transducer measurement technique is applied by: Sotgia et al. [29] and Rodriguez et al.[28].

2.5.3. Overview of different methods

To give a clear overview of all the different measurement techniques for the film thickness measurements they have been summarized in table 2.4.

Table 2.4: Overview of different measurement techniques for film measurement

Method		Intrusive	Thickness measurement range
Conductance	Probes	No	Limited (sensitivity decreases with increasing film height)
	Wires	Yes	Dependent on length of wires
Capacitance	Plates	No	Not applicable, just hold-up measurement
	Sensors	No	0.4 mm to 2.2 mm
Optical detection		No	No limit (as long as in view of camera)
PLIF		No	No limit (as long as in view of camera and in the laser laser field)

Due to the limited measurement range of the conductance probes it is not suited for this research. A non intrusive measurement is preferred, this is the reason why conductance wires are not preferred for this research. As the main objective of this research is acquiring information about the film thickness the capacitance plate measurement technique is not suited for this research. Due to the limited measurement range of the capacitance sensors and the difficulty of applying the large amount of sensors required to get good spatial results the capacitance sensor is not very suited for the current research purpose. Due to the number of adjustments required for the application of PLIF, the choice is made to use the optical detection method that does not require any adjustments to the set-up; everything required for this method was already available. This optical measurement method provides four measurement points evenly spaced apart which provide a good base for the approximation of the interface when a spline interpolation is applied.

3

Experimental set up

The experimental set up used in this experiment is present at the Process & Energy lab at the TU Delft. The set up was used prior to this experiment and has been calibrated and improved. The calibrations for the oil- and water-supply have been carried out by a previous student and will be referred to when necessary.

In this chapter the set up will be described after which the data acquisition system will be discussed and the calibration procedures for the pressure sensor and imaging.

3.1. Overview of experimental set up

The set up schematics of the front and back are shown in figures 3.2 and 3.3, respectively. The front and back side will be disused in 3.1.1 and 3.1.2.

3.1.1. Front

The front side of the set up consists of the following parts:

1. Flow loop
2. Divider

Flow loop

The flow loop is approximately seven and a halve metre long and is made of mostly PVC, the measurement section is three metre long and is made of plexiglas (PMMA); this is done for the visualisation since the plexiglas is more transparent than the PVC and increases the quality of the visual results. Near the end of this measurement pipe there are two measurement points, which are positioned at the bottom of the pipe where the water layer is thickest. The points are spaced one metre apart to measure the pressure drop over this section. Between these two points is the optical box made of PMMA where the visualisation takes place. This section of the pipe is referred to as the measurement section and is shown in figure 3.1.

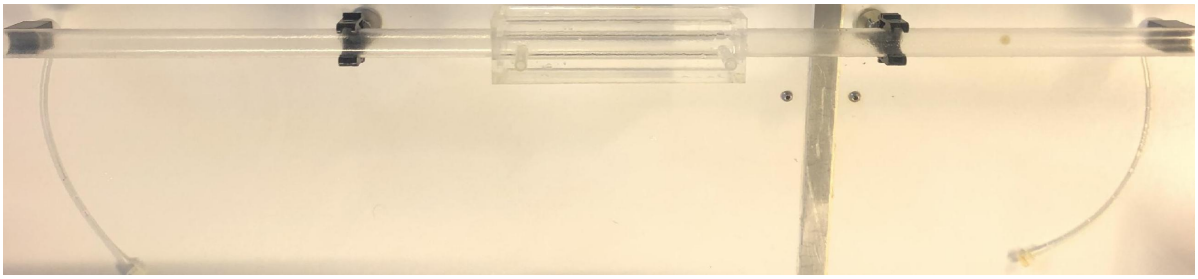

Figure 3.1: Picture of the measurement section from above

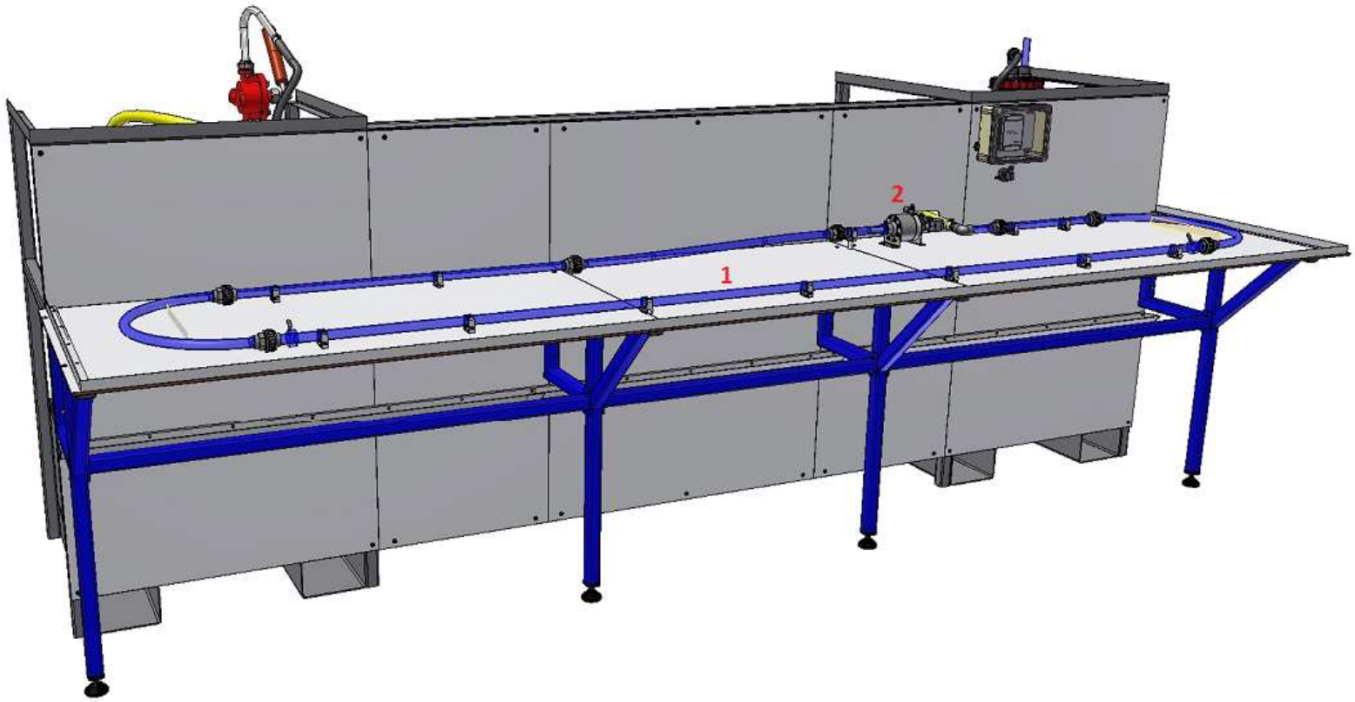

Figure 3.2: Schematic of the front of the experimental set up

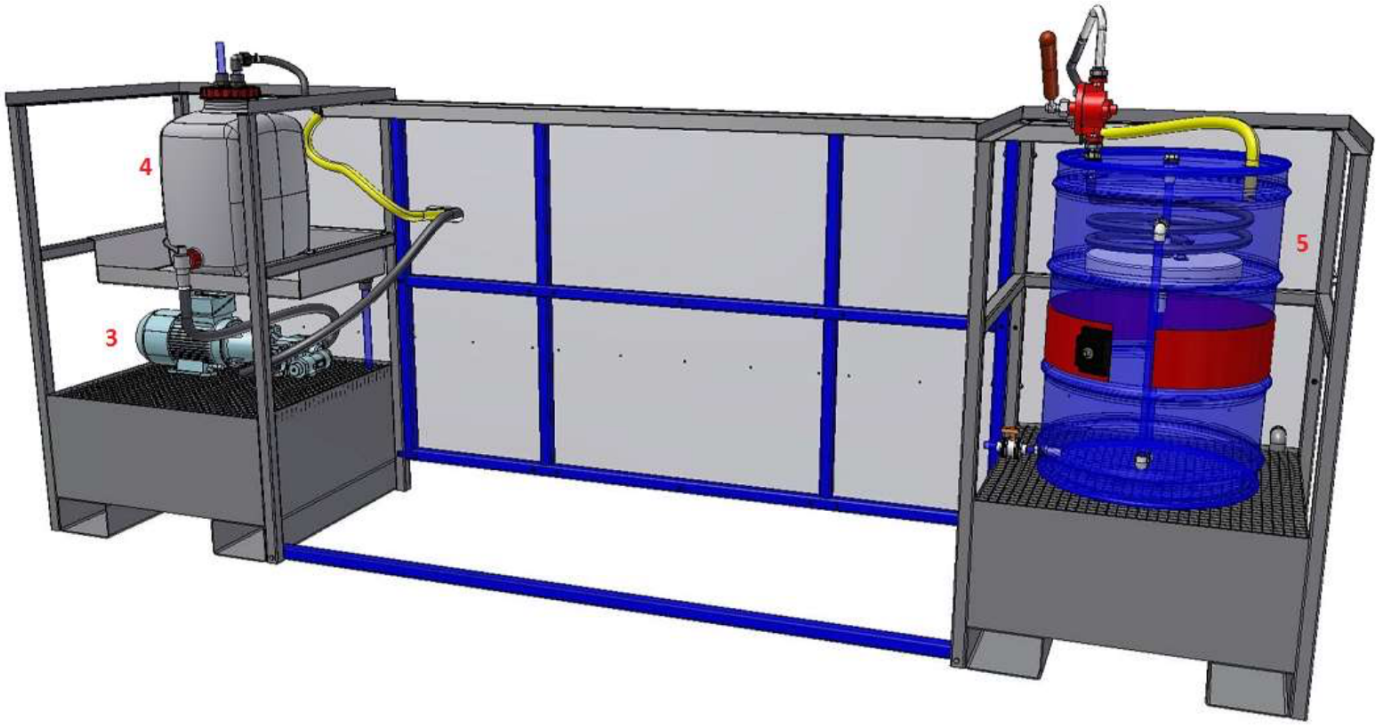

Figure 3.3: Schematic of the back of the experimental set up

Divider

In the divider oil and water are added together, the oil is added through a concentric pipe within the pipe of the flow loop. In the annulus surrounding this pipe the water is added in order to create core annular flow. A schematic of the divider is given in figure 3.4.

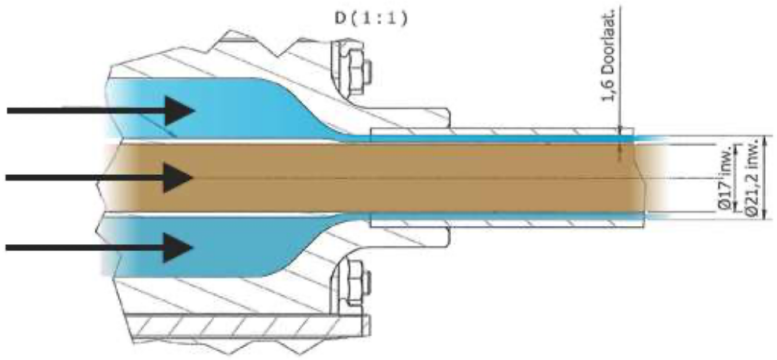

Figure 3.4: Schematic of the divider oil is brown and water is blue

3.1.2. Back

The back side of the set up consists of the following parts:

1. Heavy duty gear pump
2. Oil tank and heating system
3. Separation barrel
4. Rinsing system
5. Dump vessel

Heavy duty gear pump

The heavy duty gear pump uses three phase power to pump the oil from the reservoir into the flow loop through the divider. The pump is attached to a three way valve which can either be set to circulate the oil through the reservoir or to pump the water into the flow loop.

Oil tank and heating system

The oil tank is a 60 litre storage tank where the oil is stored prior to the experiment. In the tank there is a copper coil attached to a heating system which can be used to heat up the oil to change the viscosity of the oil. The heating device attached to the storage tank uses hot water which goes through the coper pipe to heat up the tank content. An external thermometer is inserted into the tank to measure the temperature.

Separation barrel

At the end of the flow loop there is a three way valve which will either send the content of the flow loop to the rinsing tank or the separation barrel. The separation barrel is an approximately 200 litre barrel where the oil-water mixture from the experiment is separated. Inside the barrel there is a floater which is attached to a small electrical gear pump which pumps the oil back to the oil tank. At the bottom there is a drain valve which is used to dispose of the excess water in the tank after the oil has been pumped back to the tank.

The driving force behind the separation is the density difference between the oil and water. Oil has a lower density than water making the oil float on top of the water. The time it takes for the mixture to fully separate can be calculated by modelling the oil as spherical droplets of diameter D_{e} and applying a force balance where the drag force is acting downward and the net buoyancy force acting upwards as shown in figure 3.5.

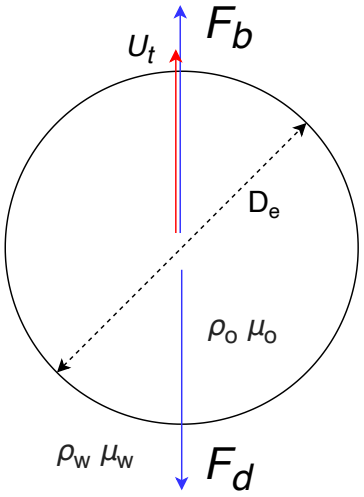

Figure 3.5: Force balance on spherical bubble

The buoyancy force and drag force are defined as follows:

$$F_b = |\rho_{\mathrm{o}} - \rho_{\mathrm{w}}| g \frac{\pi D_{\mathrm{e}}^3}{6} \tag{3.1a}$$

$$F_d = \frac{1}{2} C_d \frac{\pi D_{\mathrm{e}}^2}{4} \rho_{\mathrm{o}} U_{\mathrm{t}}^2 \tag{3.1b}$$

For the drag coefficient the results of classic stokes flow around a "fluid sphere" are used the derivation for this can be found in the book of Batchelor [6] leading to equations 3.2:

$$F_{\mathrm{d}} = 3\pi\mu_{\mathrm{o}} D_{\mathrm{e}} U_{\mathrm{t}} \left(\frac{2/3 + \kappa}{1 + \kappa} \right) \quad \& \quad C_{\mathrm{d}} = \frac{24}{Re_D} \left(\frac{2/3 + \kappa}{1 + \kappa} \right) \tag{3.2a-b}$$

Because of the high viscosity ratio these equations can be simplified to:

$$F_{\mathrm{d}} = 3\pi\mu_{\mathrm{w}} D_{\mathrm{e}} U_{\mathrm{t}} \quad \& \quad C_{\mathrm{d}} = \frac{24}{Re_D} \tag{3.3a-b}$$

This leads to a relation between the settling velocity and the diameter of the bubble:

$$U_t(D_e) = \frac{|\rho_{\mathrm{o}} - \rho_{\mathrm{w}}| g D_{\mathrm{e}}^2}{18\mu_{\mathrm{w}}} \tag{3.4}$$

The height of the oil layer is approximately 30 cm. Oil droplets with a diameter of 0.5 mm and larger are separated within 22 hours.

Rinsing system

The rinsing system (not displayed on figure 3.3) was added by Ingen Housz and improved by Van Duin. This rinsing system consist of a rinsing tank, a boiler and a pump. This way hot water can go through the flow loop with a high flow rate making the cleaning of the flow loop more practical. The rinsing is necessary to remove oil which might have fouled the walls of the flow loop and maintain similar conditions throughout the experiments.

Dump vessel

Not shown in the schematic is the 1000 litre dump vessel which is used to dispose of the water of the separation barrel and the rinsing system. Since the water might be contaminated with the oil used in the set up it needs to be disposed accordingly. This dump vessel is on the ground floor and initially the water was disposed by gravity but since the setup was moved to the ground floor, another pump was installed to dispose this waste water.

3.2. Data Acquisition System

LabVIEW by national instruments is used to monitor the experiments and collect and process the data from the different sensors in the set up.

To interpret the measurements done by the sensors, analogue signals are sent from the sensors to the data acquisition device (DAQ) which transforms the analogue signals into digital signals and writes the data related to these signals into a .lvm file.

3.3. Sensors

There are five sensors which measure flow parameters and four more safety sensors. All these sensors will be discussed shortly; the pressure sensor will be described in more detail in the next section. Most of these sensors were calibrated by Ingen Housz and this process is described in his thesis [20].

3.3.1. Oil flow rate

The specifications of the oil pump suggest a linear relation between the frequency applied and the oil flow rate. Through this linearity between the flow rate and the frequency the oil flow rate can be controlled. The calibration was carried out by Ingen Housz and his calibration has been incorporated into the data acquisition system. For more information on the calibration process consult the thesis of Ingen Housz [20].

3.3.2. Water flow rate

The water flow rate is monitored by a BIOTECH turbine flow meter which is placed between the tap water connection and the divider. The water flow rate is controlled through a valve.

The flow meter gives 1150 pulses per litre, which comes down to $8.7 * 10^{-4}$ l/pulse. These pulses are recorded by LabVIEW and converted into a volumetric flow rate. The calibration test from Ingen Housz has shown that there is a deviation of 4% between the measured and real water flow rate.

3.3.3. Oil thermometers

The oil temperature is measured at two points: once in the reservoir and again before it enters the divider. This measurement is done in order to monitor the temperature of the oil entering the set up. Since there is a direct relation between the temperature and the viscosity, the viscosity can be determined from this temperature measurement. Both thermometers give an analogue signal which is interpreted by LabVIEW and translated into a temperature.

3.3.4. Safety sensors

To ensure process safety there are four sensors which monitor the experiment. These sensors are also connected to the DAQ and can be monitored in LabVIEW. These sensors will be discussed shortly.

Manometer

A manometer is placed before the divider to monitor the pressure at this point. When the pressure exceeds a certain value the oil pump is automatically shut down to prevent damage to the set up. This sensor is linked directly to the pump and can shut down the pump autonomously and does not need LabVIEW to operate.

Level indicator oil reservoir
To prevent damage to the oil pump the oil pump automatically shuts down when the oil level in the reservoir drops below a certain point. This sensor is linked directly to the pump and can shut down the pump autonomously and does not need LabVIEW to operate.

Level indicator separation barrel
To prevent the separation barrel from overflowing there is a level indicator which gives a signal to the DAQ which in turn displays a flashing red light in the interface of LabVIEW. If this happens the flow needs to be stopped in order to prevent the separation barrel from overflowing.

Level indicator dump vessel
To prevent the dump vessel from overflowing a level indicator is placed in the dump vessel and monitored the same way as the level indicator of the separation barrel. If the level indicator gives an error the dumping of contaminated water needs to stop immediately and the dump vessel needs to be replaced by a new one.

3.4. Pressure sensor
The pressure sensor used in this experiment is a validyne DP15. This is a differential pressure transducer which measures the pressure difference over the measurement section of the flow loop. The pressure sensor is connected to a carrier demodulator which supplies power to the sensor and converts the single to an analogue signal.

3.4.1. Working principle of pressure transducer
The differential pressure transducers consists of a diaphragm of magnetically permeable stainless steel which is clamped between two blocks. In these blocks conductive coils are embedded which are connected to an E-shaped core. When the diaphragm is in its zero position the diaphragm is not deflected and it provides equal magnetic resistance between both coils. If a pressure difference is applied the diaphragm will deflect towards the cavity with the lower pressure. This will change the magnetic resistance which in turn determines the inductive value of each of the coils. A schematic of the transducer is shown in figure 3.6.

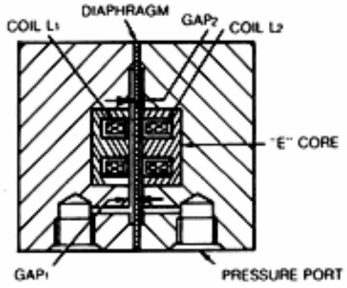

Figure 3.6: Schematic of differential pressure transducer

When the transducer is connected to a carrier demodulator the inductive change due to the pressure difference can be transformed into an AC signal which depends linearly on the pressure difference. Figure 3.7 shows the bridge formed between the transducer and the carrier demodulator.

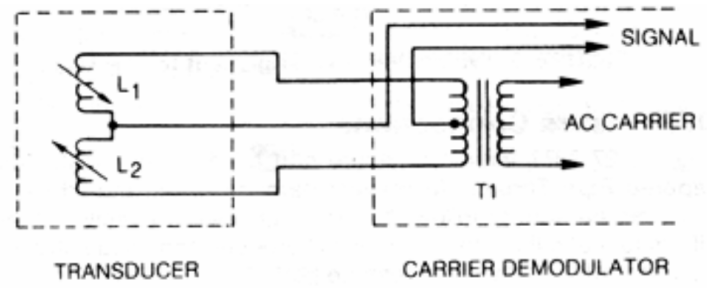

Figure 3.7: Bridge circuit between carrier demodulator and pressure transducer

The diaphragms available for the Validyne DP15 enable maximum pressure difference measurements over a wide range (860 Pa to 35 MPa)[32]; the diaphragms are capable of withstanding two times the maximum prescribed pressure difference, the signal will become non-linear after reaching the maximum prescribed load. Based on the thesis of Van Duin[34] the maximum pressure difference is known to be approximately 1.5 kPa. The choice for the 2.5 kPa is made just to be certain that the pressure drop can be measured correctly.

3.5. Visualisation

The main purpose of this experiment is to measure the film thickness on the top side of the annulus. This is done by visualising a part of the flow loop. The camera used for this visualisation is a Phantom Vision VEO 640L. A LED panel is placed behind the optical box to illuminate the measurement section so that clear images are produced.

To decrease the amount of optical distortion an optical box is attached to the measurement section as shown in figure 3.8. However, there still seemed to be some optical distortion as the analyses of the first images give some trouble and resulted in the oil core going through the inner wall in the analyses.

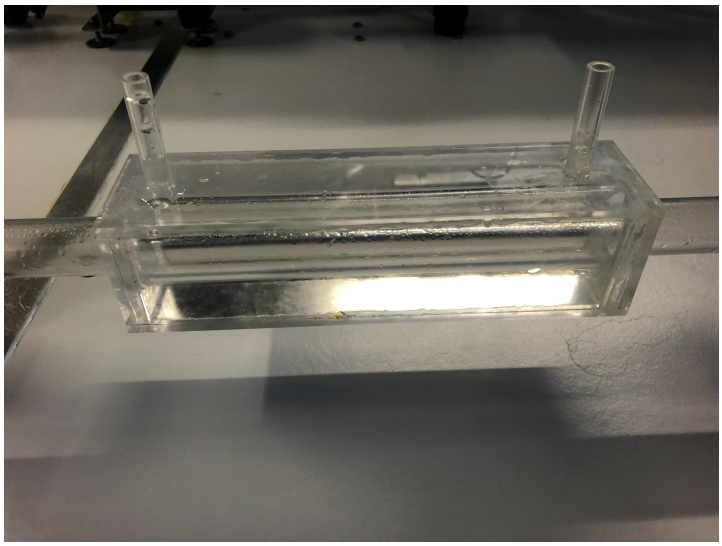

Figure 3.8: Picture of the visualisation section with optical box

4

Calibration

This chapter will explain the calibration methods used for the pressure sensor and the optical distortion.

4.1. Pressure sensor

To calibrate the pressure sensor a Martel T-140 Pressure Calibrator is used. Besides the T-140 the signal from the carrier demodulator had to be measured accurately for this purpose a multimeter is used. The set-up for the calibration is displayed in figure 4.1. First the T-140 had to be put to zero by pressing the zero button than the hose from the T-140 is attached to the DP15 and the DP15 signal goes into the carrier demodulator as described in 3.4.1. The signal outputted from the carrier demodulator goes to the multimeter so that the analogue signal can be monitored with high accuracy. The carrier demodulator settings are now changed to displayed 0.0 V at 0.0 Pa on the multimeter and T-140.

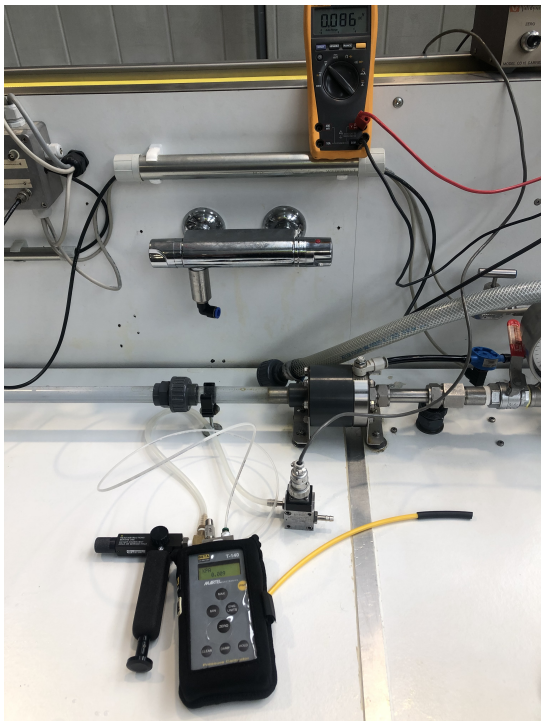

Figure 4.1: Pressure calibration set-up

Ten points are measured over the pressure range required for the experiments, which resulted in a calibration curve shown in figure 4.2.

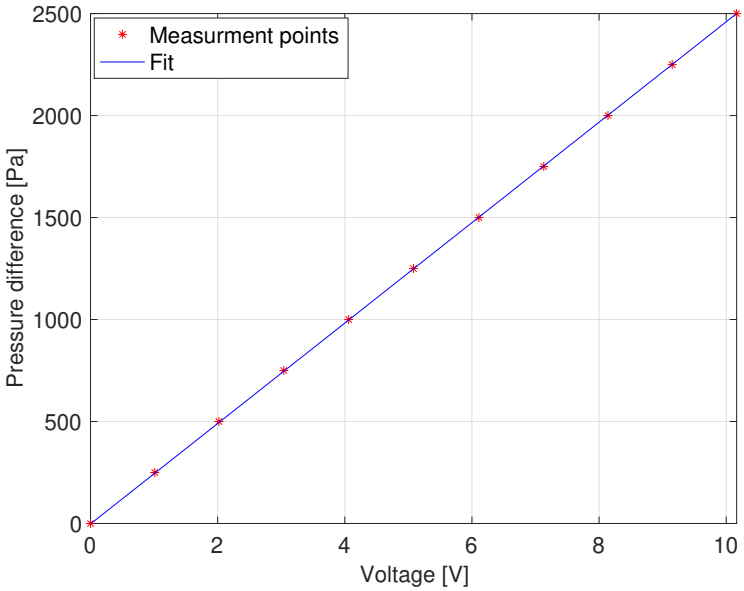

Figure 4.2: Pressure calibration

A linear relation between the voltage and pressure is acquired resulting in a perfect linear fit of $\mathrm{R}^2 = 1$. But even after this calibration a drift in the zero is noticed which might be due to atmospheric pressure changes. The maximum pressure, however, was not affected by this and the slope acquired from the calibration remains unchanged.

To account for this zero drift a zero measurement is done before every experiment resulting in the following relation between the voltage output and the pressure drop:

$$P = 246.2(V - V_0) - 2.276 \tag{4.1}$$

4.1.1. Verification

To check this calibration, single phase measurements with water are carried out and compared to the theoretical results acquired by applying the Churchill correlation for fanning friction factor[10].

$$f = 2\left[\left(\frac{8}{12}\right)^{12} + \frac{1}{(A^* + B^*)^{3/2}}\right]^{1/12} \tag{4.2a}$$

$$A^* = \left(-2.457 \ln\left[\left(\frac{7}{Re}\right)^{0.9} + 0.27\frac{k}{D}\right]\right)^{16} \tag{4.2b}$$

$$B^* = \left(\frac{37530}{Re}\right)^{16} \tag{4.2c}$$

With this relation the pressure theoretical pressure drop can be calculated by using the Darcy-Weisbach equation:

$$-\frac{\Delta P}{\Delta x} = \frac{2f\rho\bar{U}^2}{D} \tag{4.3}$$

Comparing the measurements for the calibration were compared against the Churchill correlation shown in figure 4.3.

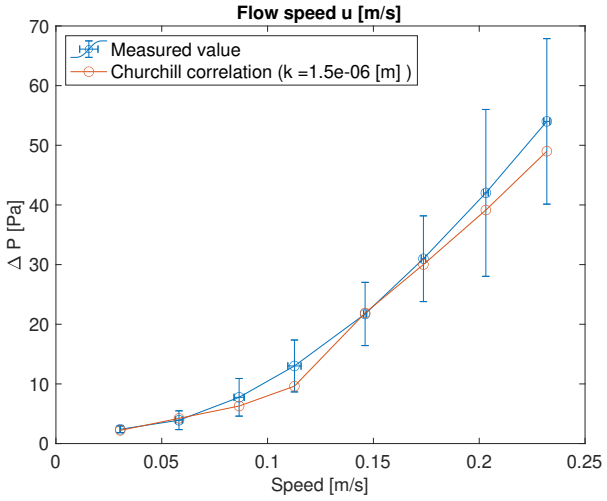

Figure 4.3: Measurements compared to theoretical results (measured over 1 metre of pipe)

4.2. Optical

Because the light has to go through several media, the light is being refracted at each intersection. As discussed in chapter 2 these refraction follow Snell's law. Since the height of the water film at the bottom is in the order of a millimetre it is important to account for this distortion of the image. A simulation of the light beams coming from within the pipe to the position of the camera was made after which an optical distortion was acquired. To verify these results a calibration pipe was made to make pictures of of the pipe with a calibration piece inside both these procedures will be described in this section.

Ray tracing analyses

For the ray tracing analyses a MATLAB script was created which calculates the angle change at the refractions and plots the final path from the centre line (x = 0) with a varying height of the the tube to the position of the camera. The results acquired from this simulation are shown in figure 4.4.

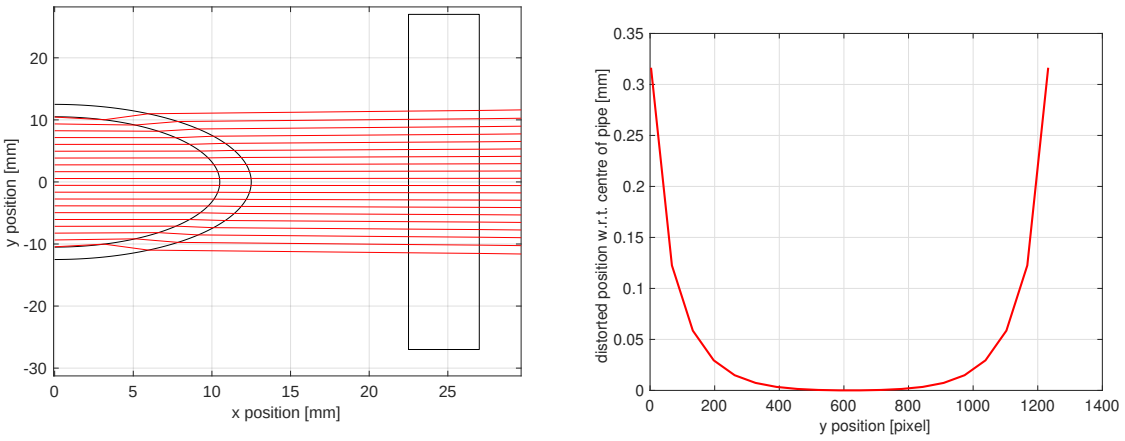

(a) Optical path

(b) Distortion as a function of pixel position

Figure 4.4: Results from simulation

The same was tried for the rays starting within the wall of the tube. that simulation, however, did converge to a solution with an imaginary part. Due to this imaginary part in in the solution, a total reflection would occur. This would mean that the incoming angle from the light ray coming from within the wall towards the inside of the tube is larger than the critical angle. It proved to be difficult to simulate this total reflection.

Verification

For the verification a calibration pipe was produced. This calibration pipe is approximately 50 cm long and has a similar optical box attached to it as the real measurement piece. There is a slid on top of the pipe section of 40 mm long with a width of two millimetre. Through this slid a calibration piece can be inserted into the pipe. A picture of the calibration piece is shown in figure 4.5.

Figure 4.5: Optical calibration pipe

Calibration target

The calibration target used is a Thor labs R2L2S3P1grid distortion target. There are dots with an equal spacing between them. This spacing is 125 µm. With this spacing there are 8 dots in the area of interest (the 1 mm closest to the inner wall). A schematic of this calibration piece is provided in figure 4.6.

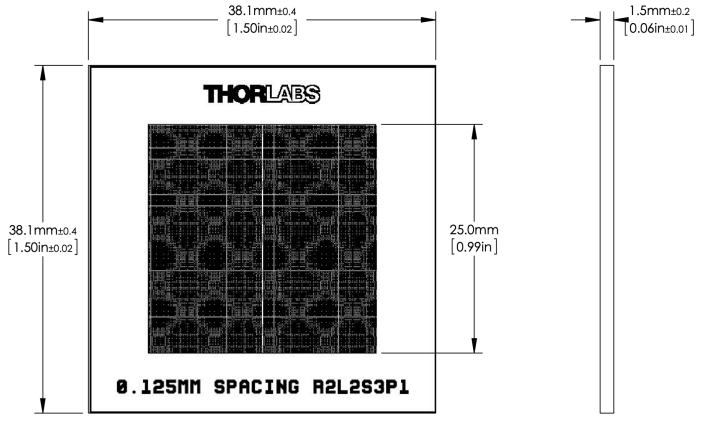

Figure 4.6: Calibration target

From these calibrations a curve is obtained which should prove that there is optical distortion close to the inner wall of the tube.

Results
The calibration image used for the verification is shown in figure 4.7. Using this image, the experimental calibration curve will be compared with the theoretical model.

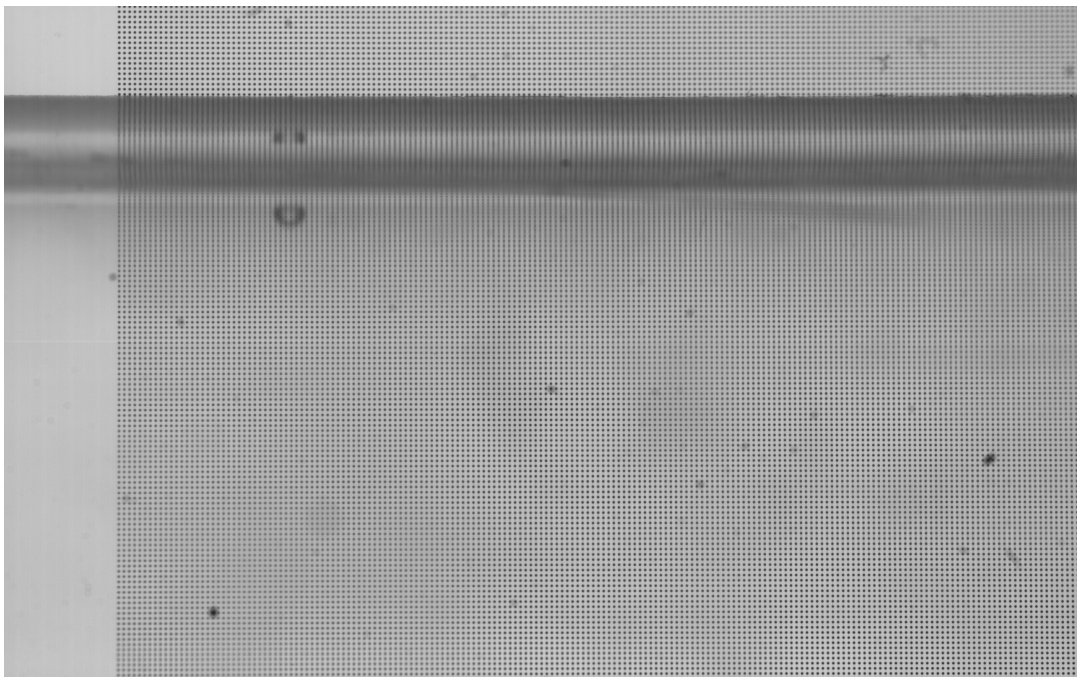

Figure 4.7: Calibration image

The spacing between the dots above the pipe outer wall is shown in figure 4.8a. From this image the spacing between the dots is derived to be 12.3 pixels which results into a ratio of $10.15\ \mu\mathrm{m/pixel}$.

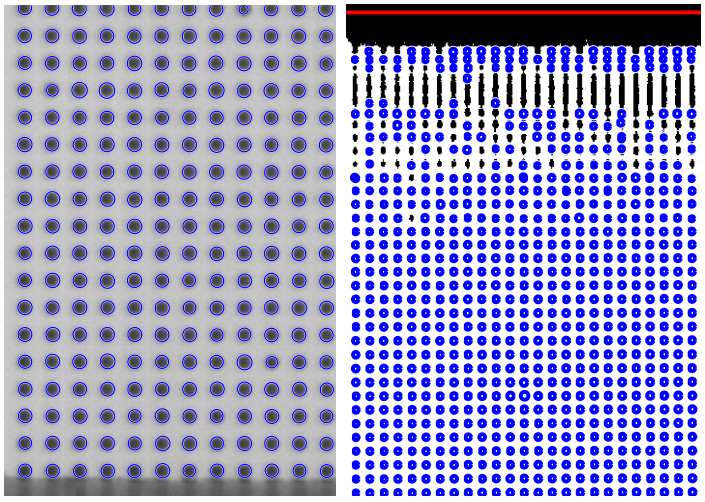

(a) Spacing above the outer wall

(b) Spacing below the inner wall the red line indicates the undistorted position of the inner wall

Figure 4.8: Results from the calibration target

To determine a relation between the pixel position with respect to the outer wall the number of pixels between two consecutive dots has to be determined. This is done with the dots detected in figure 4.8b since the real distance between the dots on the calibration target is known to be 125 µm. The relation can be determined by dividing the known distance between two dots by the number of pixels between two dots in the picture. The result of this relation is plotted in figure 4.9 where the y-axis represents the distance per pixel and the x-axis represents the horizontal pixel position with respect to the outer wall.

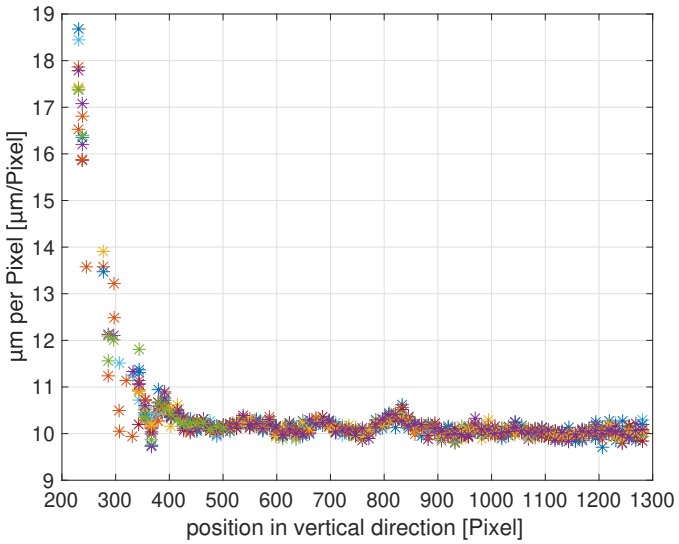

Figure 4.9: Distance between two consecutive dots versus the horizontal position

It becomes clear that the distortion occurs over the first 450 pixels. This distance corresponds to the first two millimetres from the pipe inner wall and thus the area of interest. This proves that there is some optical distortion happening in the area very close to the wall.

4.3. Comparison to ray tracing analysis

To compare the results from the calibration picture the value of interest is made dimensionless; this is done by dividing the distance covered by one pixel in the picture by the distance covered by one pixel corresponds to in the undistorted situation (above the outer wall of the tube). The result of this is shown in figure 4.10.

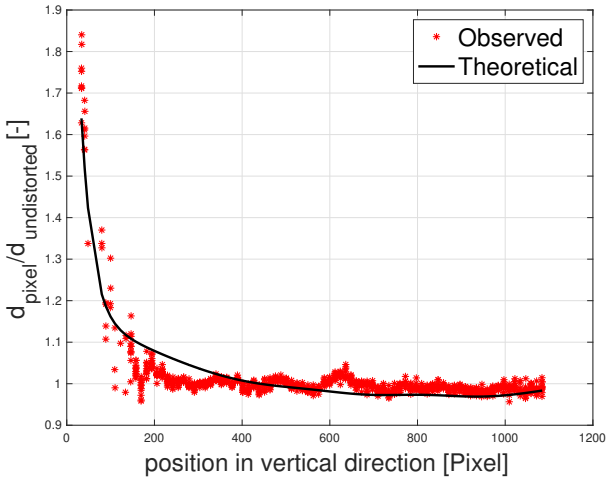

Figure 4.10: Comparison of the dimensionless enlargement compared to the undistorted pixel size

The result from the ray tracing analysis deviates from the observed distortion: the slope close to the wall is steeper in the observed result than in the ray tracing analysis. Both result types are fitted by applying a higher order Gaussian method which gives a good R^2 value. These fits have the following form:

$$f_n(x) = \mathrm{a}_1 * \exp\left(- \left(\frac{x - \mathrm{b}_1}{\mathrm{c}_1} \right)^2 \right) + ... + \mathrm{a}_n * \exp\left(- \left(\frac{x - \mathrm{b}_n}{\mathrm{c}_n} \right)^2 \right) \tag{4.4}$$

Through integration over the domain from 0 to 450 pixels the difference between the observed curve and the curve obtained from the ray tracing analysis is determined. This difference is found to be -11, which means that the ray tracing analyses underestimates the distortion by 11 pixels, corresponding to approximately 0.11 mm. The result of the ray tracing calibration curve is shown in figure 4.11b: such a calibration curve will be calculated for every experiment and will be used to process the flow pictures.

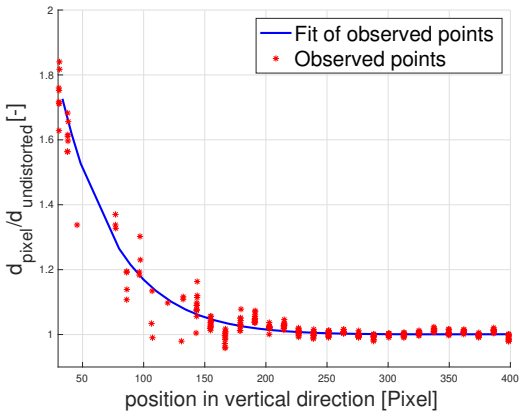

(a) Observed curve

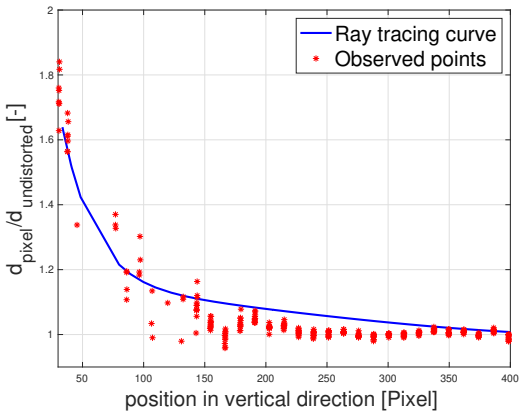

(b) Ray tracing curve

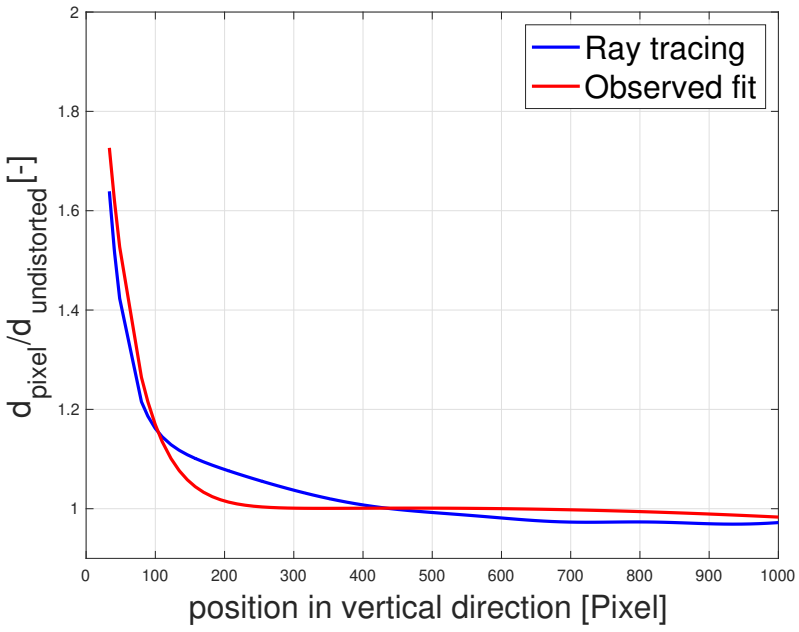

(c) Comparison between the two curves

Figure 4.11: Calibration curves comparison

4.4. Sensitivity analysis for the offset

The influence of the offset on the calibration curve will be tested. This will be done for a fixed pixel size of 17µm. The offset will be changed by increments of 0.2mm. The results are shown in figure 4.12.

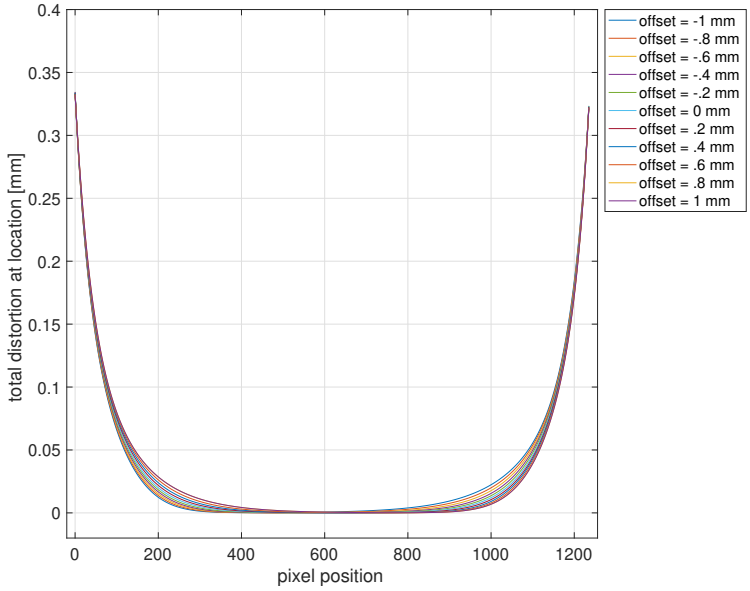

Figure 4.12: Effect of offset on the calibration curve

Figure 4.12 clearly shows that there is some deviation. To get a better understanding of the magnitude of the deviation, the extremes (± 1mm) are subtracted from the 0 offset value. The results of this are shown in figure 4.13.

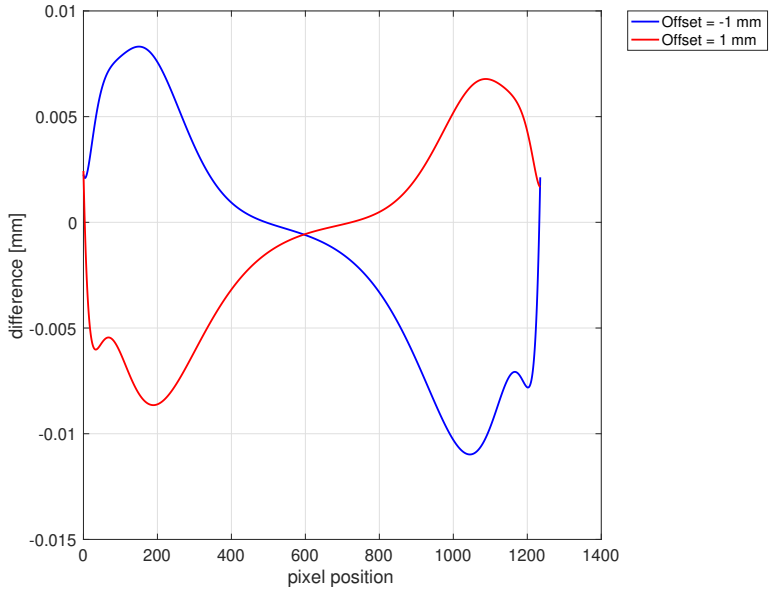

Figure 4.13: Extremes of sensitivity analyses

The largest deviation encountered is at approximately 1000 pixels from the top wall. Here a difference of -0.01 mm is found, which is roughly 1% of the total film height.

5

Processing tools

This chapter explains the process of extracting the relevant quantities from the recorded videos.

5.1. Extraction of the interface location

A typical experiment produces a film which is slightly longer than three seconds at 1020 frames per second. This gives 3066 frames that have to be analysed to get quantitative values such as the in-situ water hold-up. A typical frame from the experiment is shown in figure 5.1.

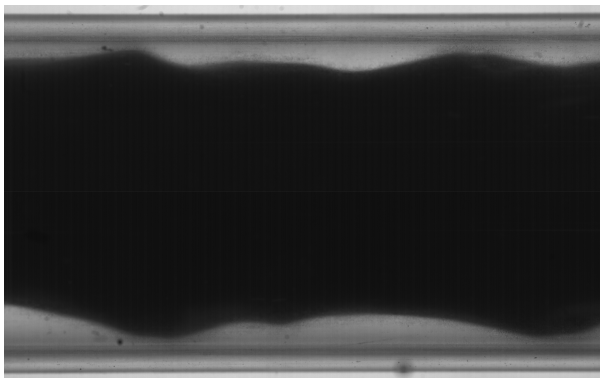

Figure 5.1: Snapshot from experiment (19.2% water cut 20°C)

The recorded image is first transformed into a black and white binary image. By applying the right threshold for the binarization function a clear image of the oil core or of the outer wall of the tube can be acquired; the resulting images are displayed in figures 5.2a and b.

(a) Black and white image of the core

(b) Black and white image of the tube as a whole

Figure 5.2: Binarized images of core and wall

Image 5.2b provides the information to determine at which pixel the outer wall is positioned. The first black pixel (top wall) and last black pixel (bottom wall) in a column are detected; this is done to determine the total width of the image. After these walls have been detected the image is checked to be horizontal; the angle of the pipe is defined as:

$$\theta = \mathrm{atan}\left(\frac{\Delta y}{\Delta x}\right)$$

where Δy is the difference between a point taken at the right end of the pipe and a point close to the left end of the pipe and Δx is simply the number of pixels in between these points in the horizontal direction. If an angle is detected the image is corrected for this angle. The undistorted pixel size is determined by dividing the pipe diameter with the number of pixels detected between the upper and lower wall. The length which one pixel represents is determined to be $17 \pm 2\mu\mathrm{m}$ throughout the experiment.

After the position of the outer wall is known, the inner wall is estimated by dividing the wall thickness (2 mm) by the pixel ratio. At this point the image of the core as shown in figure 5.2a can be analysed. The interface is detected for all the frames; this is done frame by frame in a MATLAB routine similar to the one used to detect the walls.

5.2. Correction process for optical distortion

At the start of the correction process the parameters for the Gaussian fit as described in equation 4.4. These gives the ray tracing analysis described in chapter 4 are used as input. For this it is required to analyse the two important parameters: offset and pixel size. This is done by analysing the first frame of the film of the experiment. The centre of the tube is found by detecting the upper and lower outer wall of the tube; taking the averaged value gives the position of the centre of the tube. The offset is obtained by subtracting the centre of the picture (pixels in vertical direction divided by two) from the position of the centre of the tube and the offset is obtained. The pixel size is acquired through the procedure as described previously.

This initial calibration curve gives the distorted positions, which can be used to determine the positions of the inner walls as shown in figure 5.3. This is a good way to see if the calibration curve is correct.

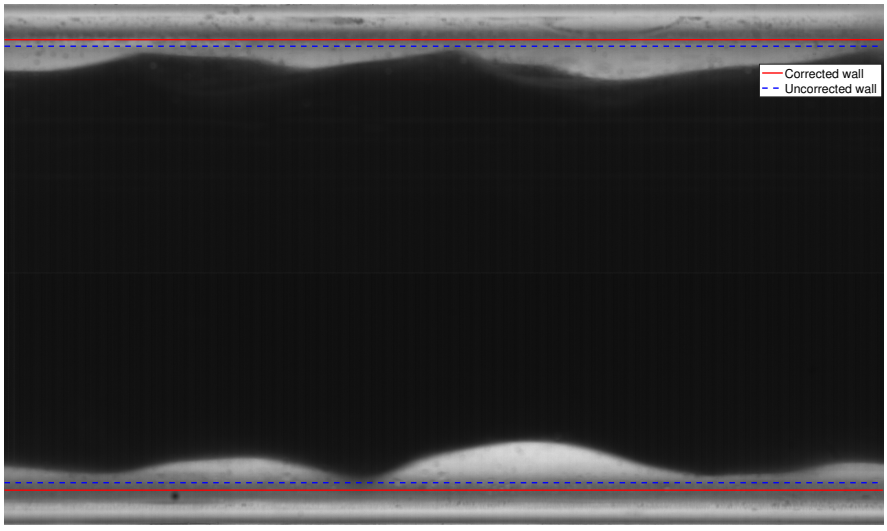

Figure 5.3: Image of the uncorrected and corrected wall where the red line is the corrected position of the wall and the dashed blue line is the uncorrected position of the wall

Through the initial calibration curve the distorted position can be determined. To obtain the undistorted

position the curve needs a small adjustment. This is done by inverting the calibration curve:

$$F^{-1}(x') = -F(x) \tag{5.1}$$

where

$$x' = x - F(x) \tag{5.2}$$

Through the calibration function described in function 5.1 the distorted position can be reverted to a undistorted position.

5.3. Results

The in-situ hold-up, wave length, wave frequency and wave speed are the variables of interest for this research. To acquire these quantities some processing actions are needed, which are discussed in this section.

5.3.1. In-situ hold-up

Averaging the position of the interface over the width of the pipe and over the time domain results in the averaged film height of the annulus at their respective positions. From these averaged film heights the in-situ hold-up can be calculated. This is done by applying a spline function to the four points. This results in a circular-like shape, which represents the area that oil core occupies within the pipe. Dividing this area of the core by the total cross-sectional area of the pipe results in the oil hold-up fraction. An example is shown in figure 5.4.

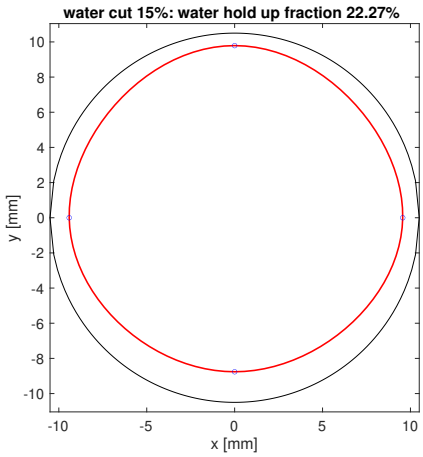

Figure 5.4: Example of result to determine the oil hold-up

5.3.2. Wave information

The important wave information consists of the wave length, wave frequency and wave speed they are related through these identity:

$$\text{wave frequency} * \text{wave length} = \text{wave speed} \tag{5.3}$$

The wave frequency and dominant wave length can both be identified by using an autocorrelation on the identified positions of the interface. The local maximum in th auto correlation function will mark the dominant wave length and frequecy. An example of the results obtained from this analysis is shown on the next page in figure 5.5.

The top figure of figure 5.5 is a snapshot of the interface at a fixed spatial position within the tube. In the example we see that the snapshot is taken from 1 to 1.1 seconds. The symbols indicate the measured points. Here we see that the period found from the autocorrelation is also present in the interface structure. The bottom graph of figure 5.5 represents the autocorrelation in which the x axis shows the wave period given in s. The first peak in this figure represents the wave period which for this example is found to be at 0.007843 s, which corresponds to a wave frequency of 128 Hz.

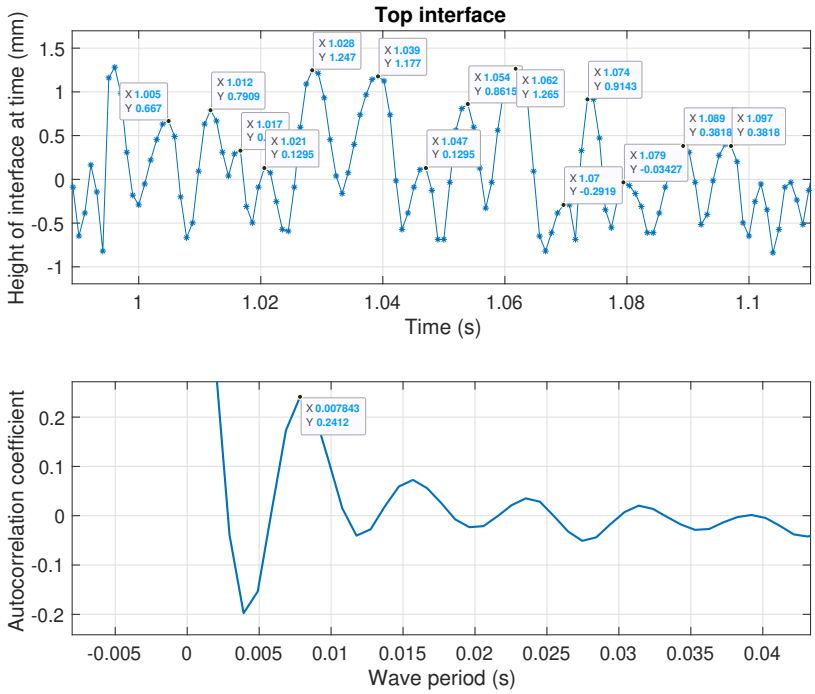

Figure 5.5: Example of frequency correlation

By applying this same procedure to the spatial domain, the wave lengths present in an image can be detected. This is done for every image in the recorded movie. In this way all the wave lengths could be detected by the autocorrelation. From these wave lengths the dominant wave length is found by looking for the value which is most often detected.

6

Results

This chapter is divided into two sections: one on the pressure drop measurements and one on the visualisation results. All the results will be discussed here and conclusions will be provided in chapter 7.

6.1. Pressure drop

Most of the pressure drop measurements were done at room temperature to compare to the results of van Duin [33] and Ingen-Housz [20]. Later experiments were done at 40°C to compare to simulations done by a PhD candidate Haoyu Li.

6.1.1. Experimental conditions

The lab measurements were carried out for the conditions displayed in table 6.1

Table 6.1: Experimental conditions

Parameter	Value	unit
Oil flow rate	0.35	[l s^{-1}]
Water cut	10, 15, 20	[%]
Oil Temperature	20, 40	[°C]

Because the experiments of Ingen Housz used an oil with a slightly lower oil viscosity and density, the results will be scaled by the pressure drop of single phase oil flow. This is done in order to make a comparison between the the work done at this set-up.

6.1.2. Scaled pressure drop

Since the oil has a very high viscosity, the single phase oil flow is laminar which significantly reduces the difficulty of calculating the pressure drop. The single phase oil flow is calculated by applying the Darcy–Weisbach equation while, as previously mentioned, the flow is laminar and thus a simple equation is acquired with known parameters.

$$\left(\frac{\Delta P}{L}\right)_o = \frac{128}{\pi}\frac{\mu_o Q_o}{D^4} \tag{6.1}$$

Which leads to the scaled pressure drop as:

$$\frac{\left(\frac{\Delta P}{L}\right)_{CAF}}{\left(\frac{\Delta P}{L}\right)_o} = \frac{\Delta P_{CAF}}{\Delta P_o} \tag{6.2}$$

6.1.3. Comparison of results

For the comparison of the results it is important to note two things: first that Ingen Housz used another oil (S4 B680) which is no longer available and second that the pressure drop measurement is done with an inverted U-tube. A comparison between the oils used is shown in table 6.2.

Table 6.2: Comparison between S2 and S4 at room temperature (20°C)

	S2 B680	S4 B680	Difference	Unit
Density	860	910	5.8%	$kg\,m^{-3}$
Viscosity	2910	3300	13.4%	cSt

Using the scalable pressure drop, a comparison is made with the results obtained in the previous studies. The comparison is shown in figure 6.1

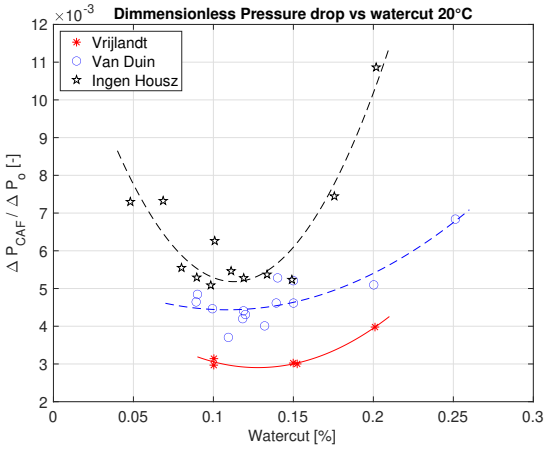

Figure 6.1: Comparison of the 20 °C measurements with Van Duin [33] and Ingen Housz [20]

In the experiments by Van Duin and Ingen Housz, the dimensionless pressure drop increases when the water cut is decreased below about 10%. An increasing dimensionless pressure drop is found after passing the 10% water cut. This trend was also found during the current experiments. The difference between the dimensionless pressure drops might be explained by the fact that there was a deviation between the measured oil viscosities of Van Duin and the current experiment. This deviation was found to be largest at 10 °C and becomes less with increasing temperature until it hits a minimum at 40 degrees after which it starts to deviate more again a comparison between the measured viscosities is shown in figure 6.2.

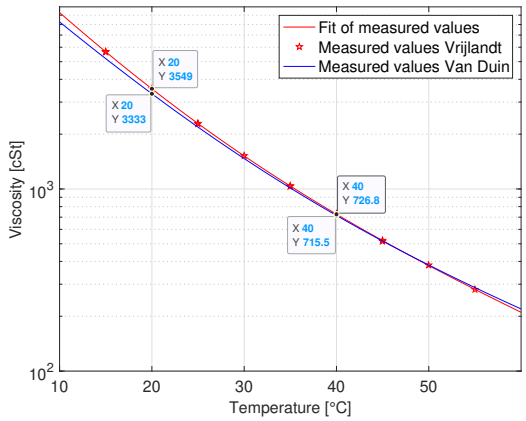

Figure 6.2: A comparison between the measured viscosity of Van Duin and the current study

Another reason for the difference might be the new pressure transducer calibration used. Whereas Van Duin used an inverted U-tube to calibrate the pressure transducer, the current experiment uses a Martel T-140 Pressure Calibrator to achieve a more accurate calibration of the pressure transducer. Since Ingen Housz did not do measurements for increased temperature, the results for 40 °C can only be compared to those of Van Duin.

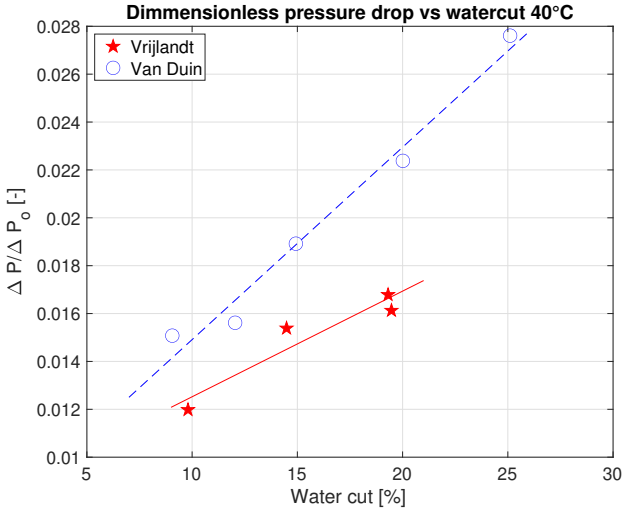

Figure 6.3: Comparison of the 40 °C measurements with Van Duin [33]

It is again found that there is a difference with the results of Van Duin but it can also be seen that the difference with the results of Van Duin has decreased. This might be due to the fact that the aforementioned deviation of the measured viscosity for this temperature is significantly less between the two studies.

Figure 6.4 compares the experimental results for the pressure drop with CFD simulations as recently carried out in the PhD project of Haoyu Li.

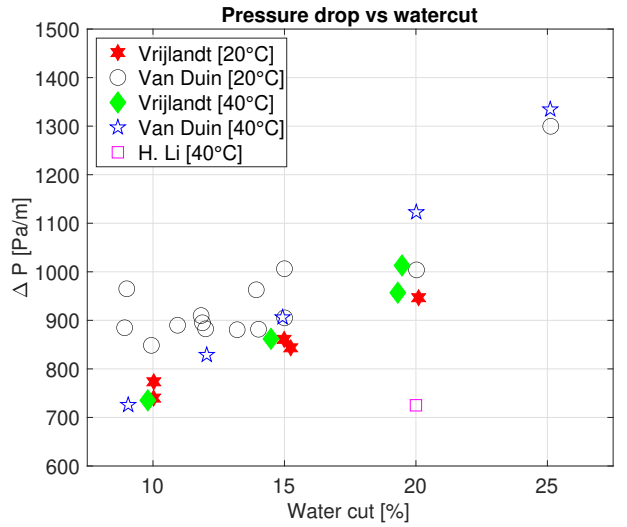

Figure 6.4: Comparison between the experiments, Van Duin and simulation by H. Li

It is seen that Van Duin structurally measures a higher pressure drop than what has been obtained during the current research. The simulation of Haoyu Li gives a pressure drop of 725 Pa at a 20% water cut, which is roughly 25% lower than what either Van Duin or the current research has shown.

6.1.4. Comparison to Ullmann and Brauner

The experimental results are compared with the predictions from the twophase model of Ullmann and Brauner [31] which is explained in 2.3.1. The results are shown in figure 6.5. In this figure each colour represents a different experiment; the filled marker is the measured value and the open marker is the value predicted by the Ullmann and Brauner model.

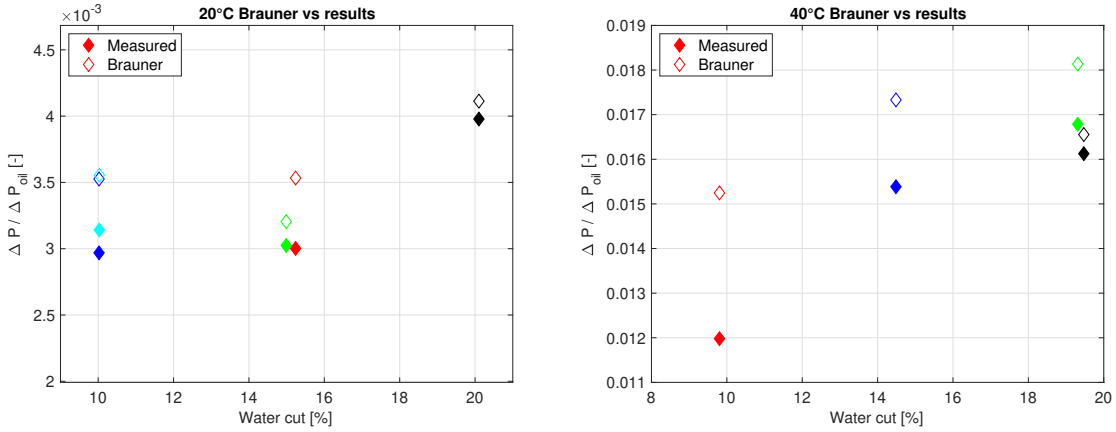

(a) 20°C (b) 40°C

Figure 6.5: Comparison of the pressure drop measurements with the model of Ullmann and Brauner

The pressure drop predictions with the model of Ullmann and Brauner are in good agreement and show a similar trend. However, the model seems to slightly overestimate the pressure drop. This also becomes clear when the scaled pressure drop from the predictions and experiments are plotted against each other, as is done in figure 6.6. Here the solid line indicates a perfect agreement with the Ullmann and Brauner model and the dashed lines indicate the $\pm 20\%$ agreement.

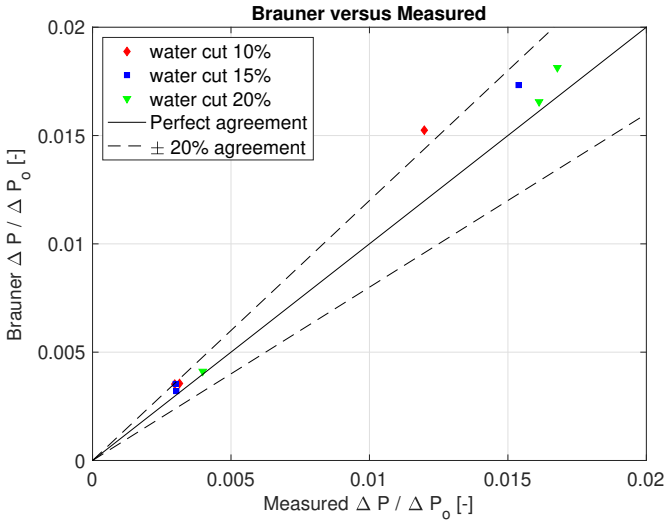

Figure 6.6: Comparison of scaled pressure drop to Brauner

The figure shows that all the pressure drop predictions with the Ullmann and Brauner model are less than 20% above the experiments. An exception is the low viscosity case at 10% water cut for which the model gives a more than 20% over prediction.

6.2. Visualisation

In this section the results from the movies recorded with the high speed camera are presented. The results as processed with the spline function algorithm can be found in appendix C. The experimental results are acquired that are shown in table 6.3. Both the raw data and the data after distortion correction are included in the table.

Table 6.3: Visualisation results

Experiment	I	II	III	IV	V	VI
Temperature		$20°C$			$40°C$	
water cut	10%	15%	20%	10%	15%	20%
Film height [mm]						
Raw						
Top	0.74	1.00	1.38	0.52	0.71	1.17
Bottom	0.89	1.30	1.76	1.06	1.74	1.72
Left	0.81	1.06	1.34	0.89	1.09	1.48
Right	0.84	1.07	1.23	0.74	0.94	1.23
Processed						
Top	0.59	0.90	1.26	0.35	0.55	1.06
Bottom	0.75	1.18	1.68	0.93	1.67	1.63
Left	0.84	1.02	1.23	0.75	0.97	1.38
Right	0.67	0.89	1.12	0.60	0.81	1.11
In-situ hold-up and hold-up ratio [-]						
Raw						
α_{w}	0.17	0.22	0.27	0.16	0.22	0.27
α_{o}	0.83	0.78	0.73	0.84	0.78	0.73
H	1.87	1.59	1.54	1.77	1.56	1.52
Processed						
α_{w}	0.16	0.21	0.26	0.15	0.21	0.26
α_{o}	0.84	0.79	0.74	0.85	0.79	0.74
H	1.73	1.47	1.44	1.61	1.45	1.49
Arney [-]						
α_{w}	0.13	0.20	0.25	0.13	0.20	0.25
α_{o}	0.87	0.80	0.75	0.87	0.80	0.75
H	1.36	1.37	1.38	1.36	1.37	1.38
Ullmann and Brauner [-]						
α_{w}	0.12	0.17	0.23	0.12	0.17	0.23
α_{o}	0.88	0.83	0.77	0.88	0.83	0.77
H	1.17	1.18	1.21	1.21	1.09	1.20

It is clear that the viscosity has almost no effect on the in-situ hold-up. Even though there is a large difference in viscosity the in-situ hold-up is almost identical. The model of Ullmann and Brauner model seems to under predict the in-situ water hold-up, This could be caused by a wrong Ci value for the slip or because of the fact that the model uses a concentric core. By comparing the results from the experiment with those predicted by Arney's empirically based model, we see that the values of Arney are very close to the measurements. In fact, the values of Arney are slightly lower than those recorded.

It is clear that the lower density at $40°C$ causes the top layer to become thinner due to a more dominant buoyancy force. Surprisingly, the thickness of the left and right water layers is not the same. These will probably become more identical if the sample size (movie length) is increased. However the internal storage of the high speed camera did not allow for this.

6.2.1. Characteristics of the interfacial waves

From the visualisation data the wave length and wave frequency can be extracted by looking at the correlation of the position of the wave, which was described in detail in chapter 5. The results obtained with the autocorrelation algorithm are presented in table 6.4.

Table 6.4: Wave characteristics of corresponding experiments

Experiment	I	II	III	IV	V	VI
Temperature		$20°C$			$40°C$	
Water cut	10%	15%	20%	10%	15%	20%
Wave length [mm]						
Top	13.0	13.7	18.3	5.5	8.8	9.7
Bottom	11.9	14.8	15.7	8.5	14.7	12.3
Left	14.4	15.9	23.0	9.1	9.8	12.0
Right	17.4	17.0	17.8	7.6	9.8	12.0
Wave frequency [Hz]						
Top	72.9	78.5	68.0	170.0	145.7	127.5
Bottom	72.9	72.9	68.0	113.3	85.0	92.7
Left	68.0	63.8	63.8	145.7	113.3	102.0
Right	60.0	68.0	68.0	127.5	127.5	113.3
Wave speed [m/s]						
Top	0.87	1.07	1.08	0.93	1.28	1.24
Bottom	0.95	1.08	1.24	0.96	1.25	1.14
Left	0.98	1.02	1.46	1.33	1.11	1.22
Right	1.04	1.16	1.21	0.97	1.25	1.36

The measured wave speed is for most cases very close to the velocity of the core. The latter can be estimated with the following equation:

$$U_{core} = \frac{Q_o}{\pi * (d_{core}/2)^2} \tag{6.3}$$

Where d_{core} is estimated through:

$$d_{core} = \sqrt{(1 - J_w) d_{in}^2} \tag{6.4}$$

With this equation a rough estimate for the core velocity in the range between 1.10 and 1.30 m/s is obtained.

It is clear that the higher temperature of the oil (i.e. lower oil viscosity) results in a more irregular interface, for which the waves become shorter and the frequency becomes larger. The thickness of the water layer also seems to affect the wave frequency and the wave length, which can clearly be seen for the top and bottom water layer. For the low temperature (i.e. higher oil viscosity) the waves seemed to be unaffected by the thickness of the water layer. It is interesting to see that the frequency for the bottom layer at the $40°C$ experiment increases for a higher water cut. However, when looking at the thickness of the water layer in table 6.4 the thickness is slightly higher for the 15% water cut than for the 20% water cut. This might explain why the frequency and wave length do not follow the same trend as the other points. It is unclear, however, why this happens.

6.3. Comparison between experimental and simulated results

For the base case conditions of the CFD simulations carried out by Haoyu Li some extra measurements were carried out with a slightly higher velocity. The experimental conditions for these simulations are:

Temperature = 40°C

Water cut = 20%

Total flow rate = 0.46 $l\,s^{-1}$

6.3.1. Pressure drop

The averaged measured pressure drop over two experiments is 1018 Pa/m, whereas the CFD simulation gives 725 Pa/m. The results from both experiments and the difference with regards to the simulation are shown in table 6.5.

Table 6.5: Results from experiments

Experiment [#]	Pressure drop [Pa/m]	Difference with simulation
1	1010	28%
2	1024	29%

6.3.2. Interface waves

The results for both the experiment and the simulation are given in table 6.6.

Table 6.6: Results for base case conditions

	Top	Bottom	Left	Right
Film height [mm]				
Experiment	1.18	1.62	1.46	0.98
Simulation	0.66	3.63	1.00	1.00
Difference	-44%	124%	31%	2%
Wave length [mm]				
Experiment	10.8	11.8	11.4	10.7
Simulation	17.4	24.8	23.3	23.3
Difference	61%	110%	104%	117%
Wave frequency [Hz]				
Experiment	127.5	102.0	127.5	113.3
Simulation	68.0	50.0	54.0	54.0
Difference	-47%	-51%	-52%	-58%
Wave speed [m/s]				
Experiment	1.37	1.21	1.30	1.37
Simulation	1.18	1.24	1.26	1.26
Difference	-14%	3%	-3%	-8%

There are large differences between the measurements and the CFD simulation with regard to the thickness of the film heights. The wave frequency in the simulation is approximately half that found in the measurement and the wave length is approximately twice that found in the measurements, resulting in almost identical wave speeds.

6.3.3. Hold-up ratio

The measured water hold-up fraction is 0.257, whereas the CFD simulation gives 0.255. And the measured hold-up ratio is 1.38, whereas the CFD prediction is 1.37. The determined hold-up ratio is in good agreement, however, the shape of the interfaces is not in agreement. A comparison between the interfaces is shown in figure 6.7.

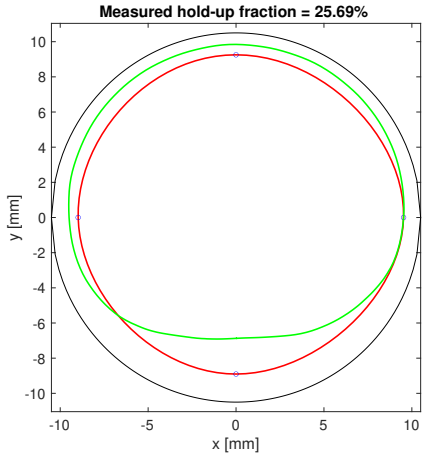

Figure 6.7: Comparison between interfaces: experiment (red) versus simulation (green)

The water hold-up fraction in the experiments is determined by fitting a spline through four measurement points for the thickness of the water annulus (at the top, bottom, left side, right side). Since the spline function is only based on four points it would be unrealistic to expect it to perfectly determine the interface. To see how well the spline function represents the interface, a comparison is made with the data from the CFD simulation. The simulation provides the exact location of the interface. The four points of the simulated interface were supplied to the spline function. The two interfaces from the simulation are compared in figure 6.8.

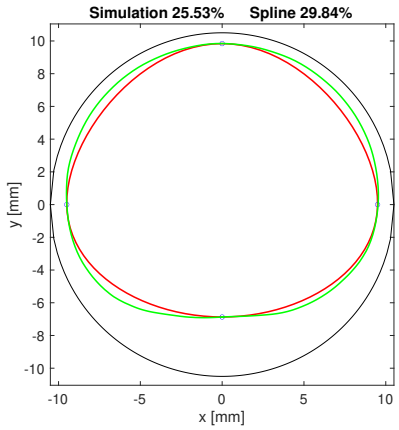

Figure 6.8: Comparison of spline function (red) and simulated interface (green)

It is clear that the spline function over predicts the water hold-up in this situation; the spline function gives 29.8% water hold-up where the simulated interface gives 25.5% water hold-up. To improve the spline function interpolation more than four points would be required.

7

Conclusions and recommendations

7.1. Conclusions

Lab experiments were carried out for horizontal core-annular flow of oil and water in a horizontal pipe with 21 mm diameter to determine the water hold-up fraction and the characteristics of the inter facial waves. This was done with the help of a high speed camera and several MATLAB routines. The oil flow rate has been kept almost constant (0.35 l/s). The water flow rate was changed from experiment to experiment, which was done to obtain different water cuts. The oil was heated to change its viscosity and to see how this affects the in-situ hold-up and wave structure. It seems that the oil viscosity has no effect on the in-situ hold-up ratio (the latter is a measure of the oil-water slip; the hold-up ratio is one if there is no slip, which is if the water hold-up fraction is equal to the water cut). However it showed that the increased density difference due to heating of the oil did make the top water layer thinner. This can be explained by the increased buoyancy force due to the larger density difference between the water and oil.

The pressure drop was measured with the same kind of pressure transducer as used in the thesis of Van Duin. A deviation of ± 70Pa was detected during the measurements which is more than the $\pm 1\%$ full scale (± 25Pa) accuracy of the device as specified by the vendor (Validyne). The pressure drop as recorded during the experiments proved to be slightly lower than what was found by Van Duin. This might be due to the fact that another calibration method is used during the current experiments; whereas Van Duin used an inverted U-tube, the present experiment used a Martel T-140 Pressure Calibrator which gives a more accurate reading for the pressure drop. This might be an explanation for the difference between the measurements of Van Duin and the current measurements.

It was also shown in the flow visualisation that the light is distorted very close to the wall of the pipe. A model that tracks the light path has been developed to estimate this distortion. That model, however, when tested for a picture with known distortion, proved to slightly underestimate the distortion very close to the wall and over estimate the distortion further away from the wall. Despite this, the model was used to derive a calibration curve that could be used to post process the recorded pictures and reconstruct the actual position of the inner pipe wall and the thickness of the water annulus. When applying the model calibration curve the wall position seemed to be correctly determined. After correction the in-situ hold-up could be determined through using a spline interpolation for the four measurement points of the thickness of the water annulus (at the top and bottom of the pipe, and at the left and right sides). Through comparison with a CFD simulation of the flow it was shown that the spline interpolation with four points gives an overestimation of the water hold-up fraction by about 24%.

The hold-up ratio is higher for a lower water cut and almost constant for the higher water cuts. The effect of the oil/water viscosity ratio was also tested from which it can be concluded that the viscosity ratio has no effect on the in-situ hold-up. However, due to the increased density difference at a lower viscosity ratio (for the higher temperature) the core moves more upward which is due to the buoyancy force. By decreasing the viscosity ratio, the waves become shorter and the wave frequency becomes larger but the wave velocity remains almost the same.

Experiments were carried out to reproduce the conditions of the CFD simulation preformed by Haoyu Li. When comparing the results of the simulation to those measured during the experiment (for 0.46 l/s total flow rate, 20% water cut, and a viscosity ratio of 600) it is found that the pressure drop determined by the simulation is roughly 30% lower than the pressure drop measured during the experiment The measured water hold-up fraction is 0.257, whereas the CFD simulation gives 0.255; however, the interfaces show significant differences the core is more concentric during the experiment than the interface determined by the CFD simulations. The comparison of the wave characteristics resulted in almost identical wave speeds, however, the wave frequency in the simulation was half that measured and the wave length in the simulation is twice that found in the measurements.

7.2. Recommendations

A solution to the problem encountered with the distortion close to the inner wall of the pipe might be the replacement of the measurement section by a thin walled glass pipe. Glass is more transparent than PMMA and can be constructed with a significantly thinner wall. This would greatly improve the optical results close to the wall. Another option for reducing the distortion would be to fill the optical box with glycerol this has a refractive index which is almost identical to that of the PMMA used for the pipe. This would give less refractions at the interfaces and therefore a smaller correction in the post processing of the pictures would be required.

It might be worth investigating the possibility to apply PLIF (Planner Laser Induced Fluorescence) as done in the thesis of Rajamani [27]. He has proven that you can measure the film height over the whole section in sight of the camera by applying this technique. This would result in a much larger amount of measurement points which could lead to a more accurate description of the water film height. If a high speed camera with more internal storage is used the averaged film heights will be influenced less by irregularities (i.e. bubbles which sometimes form on the surface) on the surface of the interface. It would also be interesting to see if the difference in the thickness of the water annulus between the right and left side decreases. Another way to measure the in-situ hold-up is by installing quick closing valves which will trap the oil and water inside of the pipe. The oil and water has to be sent to a volume measuring unit. This would require a number of adjustments to the set up but one would no longer have to deal with the optical problems that were encountered during the experiment. This approach was previously used by Charles et al. [9].

The pressure drop measurement has proven to be very sensitive. It would help to increase the length over which the pressure drop is measured. The pressure hole could be installed one meter further up stream which would increase the pressure drop by a factor of two in comparison to the other location. Therefore if the fluctuations of $\pm 70\mathrm{Pa}$ remain, the pressure drop measurement would become more accurate. However for the two metre measurement point it should first be confirmed that the flow is not affected by the bend prior to this point. It could also be an idea to add another pressure transducer to the set-up and do two measurements. One would then be the pressure drop over one metre and the other would be the pressure drop over two metre. Both these suggestions should increase the reliability of the pressure drop measurement. It is also possible to replace the current pressure drop measurement device (Validyne DP15) which has an accuracy of $\pm 1\%\mathrm{FS}$ (FS = full scale) with a device which has a higher accuracy over the FS range. A quick review showed that the SETRA 230 has an accuracy of $\pm 0.25\%\mathrm{FS}$ which is a significant increase. It also uses another measurement method than the DP15; it works on the basis of a thin flexible sheet which upon exposure to a pressure difference of the measurement section deflects slightly which changes the capacitance. This in turn creates a signal which can be interpreted in labVIEW as a pressure drop.

A

Technical data sheet of PMMA

Acrylic

Tubes & rods

TECHNICAL DATASHEET

Manufacturer/distributor: PyraSied Xtreme Acrylic

Material: Acrylic (cast and extruded) and Polycarbonate tubes and rods

Technical Properties

Typical property values
(at 20° C and 50% relative humidity)

Mechanical Properties	NORM63	Unit	Cast PMMA	Extruded PMMA	Extruded Polycarbonate
Specific weight	DIN 53479	gr/cm^3	1,19	1,19	1,19
Impact strength (Charpy)	DIN 53453	kJ/m^2	15	15	65
Notched impact strength a iN (Izod)	DIN 53453	kJ/m^2	1,6	1,6	4,5
Tensile strenght ðM	D638	Mpa			
-40° C			110	100	tbm
20° C			80	70	50
70° C			40	35	tbm
Elongation at break	DIN 53455	%	5,5	4,5	no break
Flexural strength (st. test specimen 80x10x4 mm^3)	D790	Mpa	115	105	100
Compressive yield stress	-	MPa	110	103	tbm
Max safety stress ðmax (up to 40° C)	-	Mpa	5 ... 10	5 ... 10	5 ... 10
modulus of elasticity Et (short-term value)	D790	MPa	3300	3300	2300
Indentation hardness H 961/30	DIN 53456	MPa	175	175	110
Abrasion resistance in Taber abrader test (100 rev.; 5,4 N; CS-10F)	-	% Haze	20 ...30	20 ...30	30 ...40
Coefficient of friction μ	-	-			
plastic/plastic			0,8	0,8	-
b) plastic/steel			0,5	0,5	-
c) stell/plaric			0,45	0,45	-
Poisson's ratio μ (dilatation spees of 5%/min; up to 2% dilatation; at 20°C)	-	-	0,37	0,37	-
Resistance to puck impact from thickness (FMPA Stuttgart - Germany)	similar to DIN 18032	-	12 mm	8 mm	-
Sound velocity	-	m/s	2700 ... 2800	2700... 2800	-

The norms indicated in this table are taken from:
a) DIN: German Society for Standardisation;
b) D (or ASTM): American Society for Testing Materials

S.K 07 2016

Acrylic
Tubes & rods
TECHNICAL DATASHEET

	NORM63	Unit	Cast PMMA	Extruded PMMA	Extruded Polycarbonate
Weight sounded reduction index Rw at thickness	-	dB			
4 mm			26	26	-
6 mm			30	30	-
10 mm			32	32	-
Optical Properties					
ttTransmittance ⊥D65	DIN 5036	%	~ 92	~ 92	~ 88
UV transmission	-	-	no	yes	yes
Reflection loss the visible range (each surface)	-	%	4	4	4
Adsorption in the visible range	-	%	<0,05	<0,05	-
Refractive index nD20	-	-	1,491	1,491	-
Electrical Properties					
Volume resistivity ſD	DIN VDE 0303	ohm. cm	>1015	>1015	>1017
Dielectric strength Ed (1 mm specimen thickness)	DIN VDE 0303	kV/mm	~ 30	~ 30	-
Dielectric constant	DIN 53483	-			-
at 50 MHz			3.6	3.7	
at 0,1 MHz			2.7	2.8	
Dielectric loss factor	DIN 53483	-			-
at 50 MHz			0.06	0.06	
at 0,1 MHz			0.02	0.03	
Thermal Properties					
Coefficient of linear thermal expansion	DIN 53752	mm/m ° C	0,7	0,7	0,65
Possible expansion to heat and moisture	-	mm/m	5	5	6
Thermal conductivity at 20°C	DIN 52612	W/(mK)	0,19	0,19	-
U-value for thickness:	DIN 4701	W/m2K			
1 mm.			5,8	5,8	-
3 mm.			5,6	5,6	-
5 mm.			5,3	5,3	-
10 mm.			4,4	4,4	-
Specific Heat c	-	J/gK	1,47	1,47	-
Forming temperature	-	°C	110 - 175	110 - 160	160 - 180
Max. surface temperature (IR radiator)	-	°C	200	180	-
Max. service temperature (without mech. stress)	"	°C	80	70	120

PYRASIED XTREME ACRYLIC®
☎ +31(0)58-76 76 100 ✉ sales@pyrasied.nl 🌍 www.pyrasied.nl

	NORM63	Unit	Cast PMMA	Extruded PMMA	Extruded Polycarbonate
Ignition temperature	DIN 51794	°C	425	430	-
Fire rating (material thickness > 2 mm.)	EN13501	class	E	E	Bs1d0
Heat deflection temperature under load (HDT)		°C			
deflection 1,8 MPa			105	90	
deflection 0,45 MPa			113	95	
Behavior Towards Water					
Water absorption (24 h. 20° C) from dry state; specimen 60 x 60 x 2 mm^3	DIN 53495	mg	41	38	45
Max weight gain during immersion	DIN 53495	%	2,1	2,1	2,1

Our technical advice to the uses of our materials are typical values supplied in accordance with the tests of our manufacturer and with the normally commercially acceptable standard. They are given without any obligation. The buyer is responsible for the application and processing of our products and is also liable for observing any third party rights.

PYRASIED *XTREME ACRYLIC*®
☎ +31(0)58-76 76 100 ✉ sales@pyrasied.nl 🌐 www.pyrasied.nl

B

Technical data sheet of Shell Morlina S2 B680

Technical Data Sheet

Previous Name: **Shell Morlina Oil**

Shell **Morlina** *S2 B 680*

- *Reliable Protection*
- *Industrial Application*
- *Water Shedding*

Industrial Bearing and Circulating Oils

Shell Morlina S2 B oils are high performance oils designed to provide outstanding oxidation and water separation protection for most general industrial bearing and circulating oil system applications and certain other industrial applications which do not require oils with extreme pressure (EP) properties. These oils meet the requirements of the Morgan Construction Company and Danieli for common bearing oils.

DESIGNED TO MEET CHALLENGES

Performance, Features & Benefits

- **Long oil life - maintenance saving**

  Shell Morlina S2 B oils are formulated with a well proven rust and oxidation inhibitor additive package that helps provide consistent performance and protection throughout the maintenance interval.

- **Reliable wear and corrosion protection**

  Shell Morlina S2 B oils help prolong the life of bearings and circulating systems through:

  -Excellent water separation characteristics that helps ensure that critical oil films are retained between highly loaded parts.

  -Good air release characteristics to minimize cavitation and associated damage to circulating pumps.

  -Helps protect against corrosion, oxidation, and emulsion formation, even in the presence of water.

- **Maintaining system efficiency**

  Shell Morlina S2 B oils are blended with high quality, solvent refined base oils that promote good water separation and air release to ensure the efficient lubrication of the machines and systems.

Main Applications

- **Machine circulation system**
- **Oil lubricated bearings**

  Suitable for most plain and rolling element bearings and general industrial applications.

- **Roll-neck bearings**
- **Enclosed industrial gear systems**

  Low or moderately loaded enclosed gears where EP performance is not required.

Specifications, Approvals & Recommendations

- Morgan "Morgoil®" Lubricant Specification New Oil (Rev. 1.1) (MORGOIL is a registered trademark of the Morgan Construction Company)
- Danieli Standard Oil 6.124249F
- DIN 51517-1 – type C
- DIN 51517-2 – type CL

  For a full listing of equipment approvals and recommendations, please consult your local Shell Technical Help Desk.

Compatibility & Miscibility

- **Paint Compatibility**

  Shell Morlina S2 B oils are compatible with seal materials and paints normally specified for use with mineral oils.

Typical Physical Characteristics

Properties			Method	Shell Morlina S2 B 680
ISO Viscosity Grade				680
Kinematic Viscosity	@40°C	mm^2/s	ASTM D445	680
Kinematic Viscosity	@100°C	mm^2/s	ASTM D445	37

Properties			Method	Shell Morlina S2 B 680
Density	@15°C	kg/m³	ISO 12185	910
Viscosity Index			ISO 2909	min 85
Flash Point (COC)		°C	ISO 2592	300
Pour Point		°C	ISO 3016	-9
Rust, Distilled Water			ASTM D665A	Pass
Emulsion Test - @82°C (Unless specified by *)		Mins	ASTM D1401	min 40
Oxidation Control Test : TOST		Hrs	ASTM D943	min 1000
Oxidation Control Test : RBOT		Mins	ASTM 2272	min 300
Foam Test, Seq II		ml foam at 0/10 mins	ASTM D892	20/0

These characteristics are typical of current production. Whilst future production will conform to Shell's specification, variations in these characteristics may occur. *@54°C

Health, Safety & Environment

- **Health and Safety**

  Guidance on Health and Safety is available on the appropriate Material Safety Data Sheet, which can be obtained from http://www.epc.shell.com/

- **Protect the Environment**

  Take used oil to an authorised collection point. Do not discharge into drains, soil or water.

Additional Information

- **Advice**

  Advice on applications not covered here may be obtained from your Shell representative.

Viscosity - Temperature Diagram for Shell Morlina S2 B

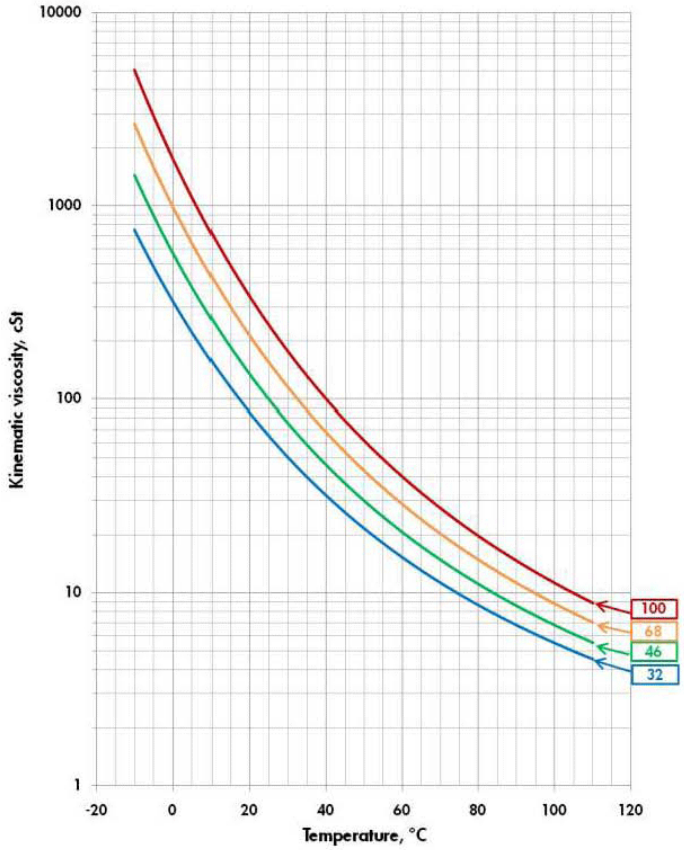

Technical Data Sheet

Viscosity - Temperature Diagram for Shell Morlina S2 B

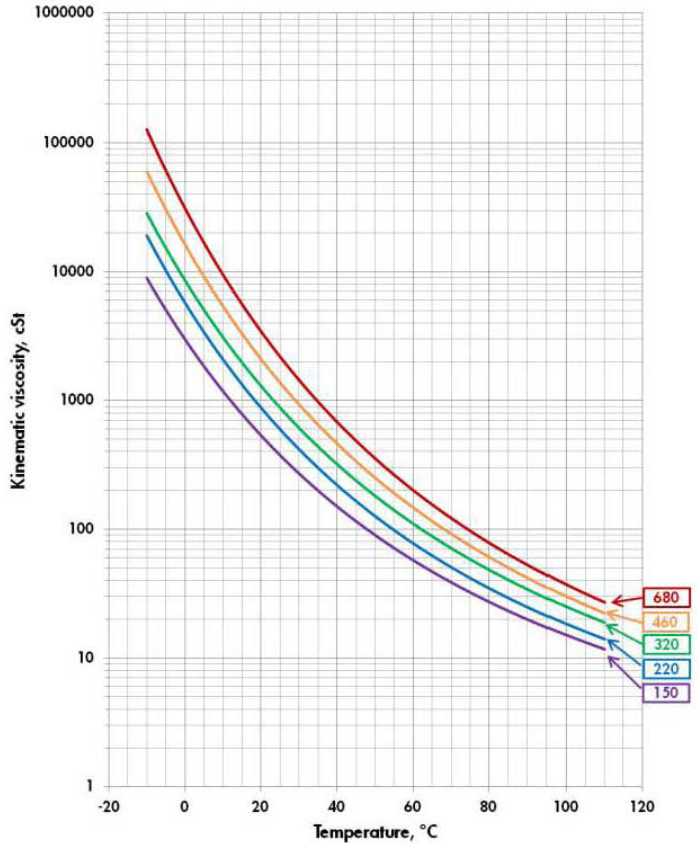

Shell Lubricants

Page 4 of 4

20/08/2012

C

Results spline function

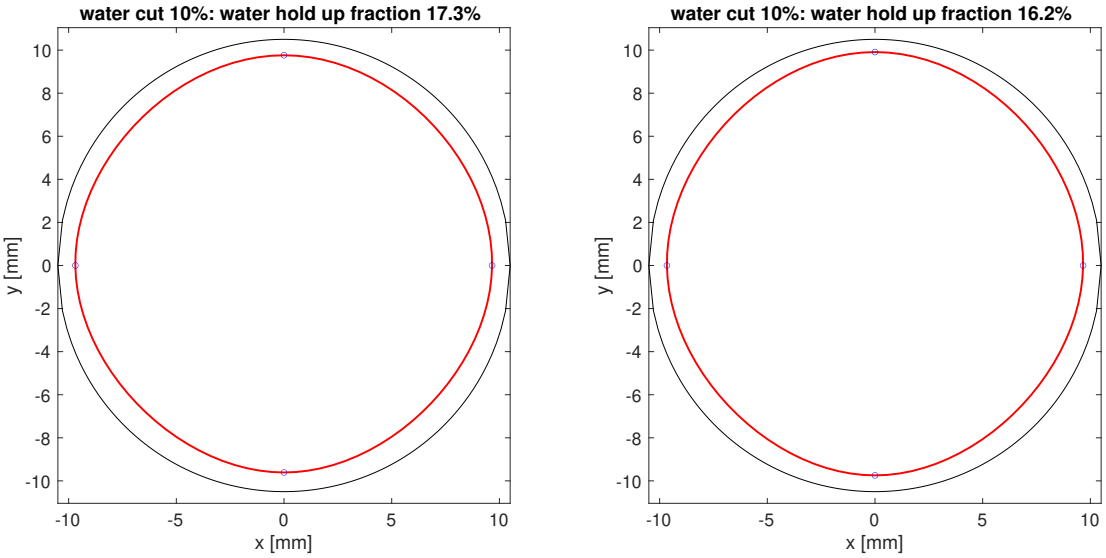

(a) Raw

(b) Processed

Figure C.1: Result of the spline function for 10% water cut and 20 °C

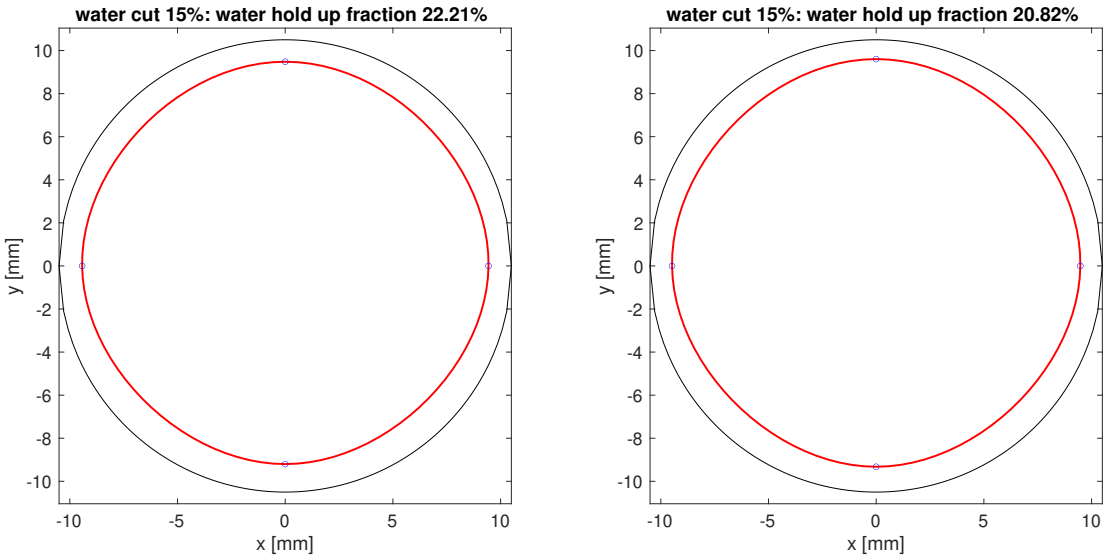

(a) Raw (b) Processed

Figure C.2: Result of the spline function for 15% water cut and 20 °C

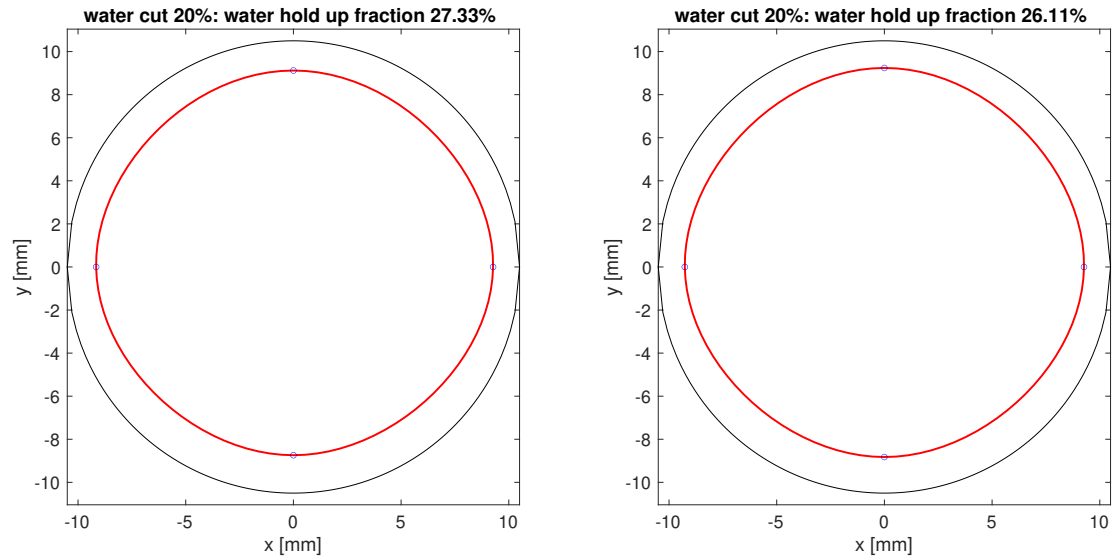

(a) Raw (b) Processed

Figure C.3: Result of the spline function for 20% water cut and 20 °C

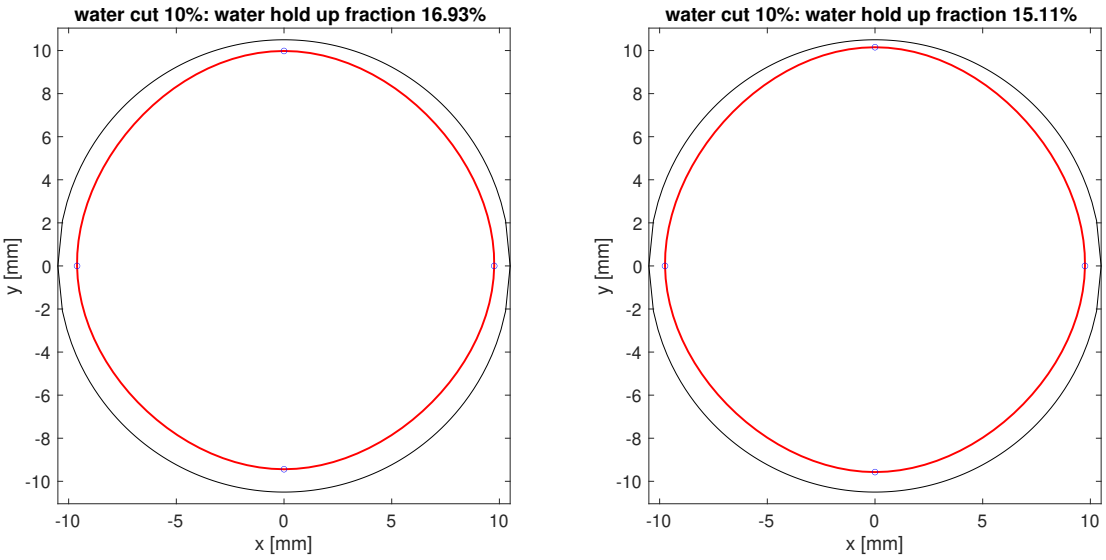

(a) Raw (b) Processed

Figure C.4: Result of the spline function for 10% water cut and 40 °C

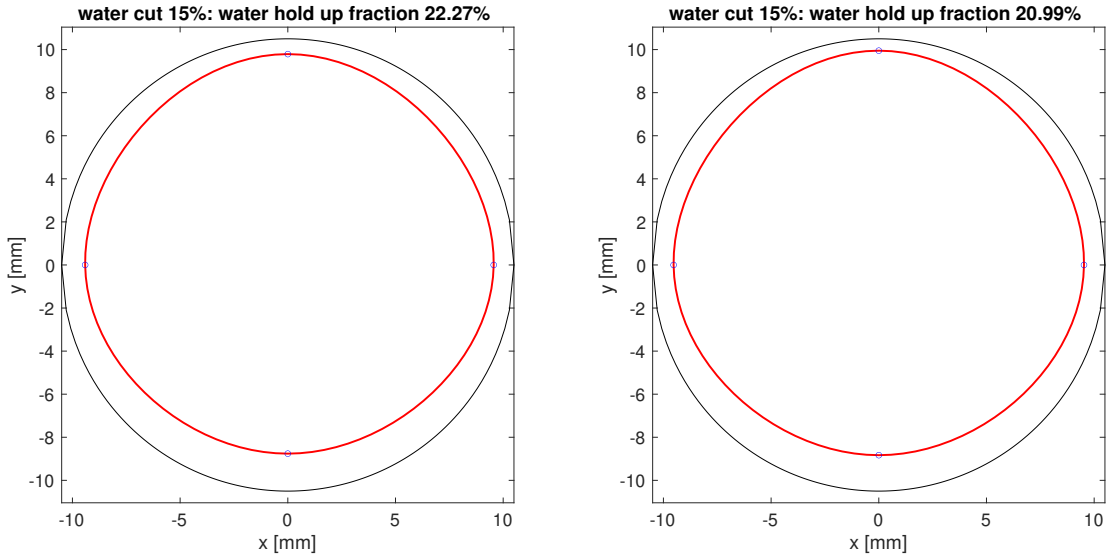

(a) Raw (b) Processed

Figure C.5: Result of the spline function for 15% water cut and 40 °C

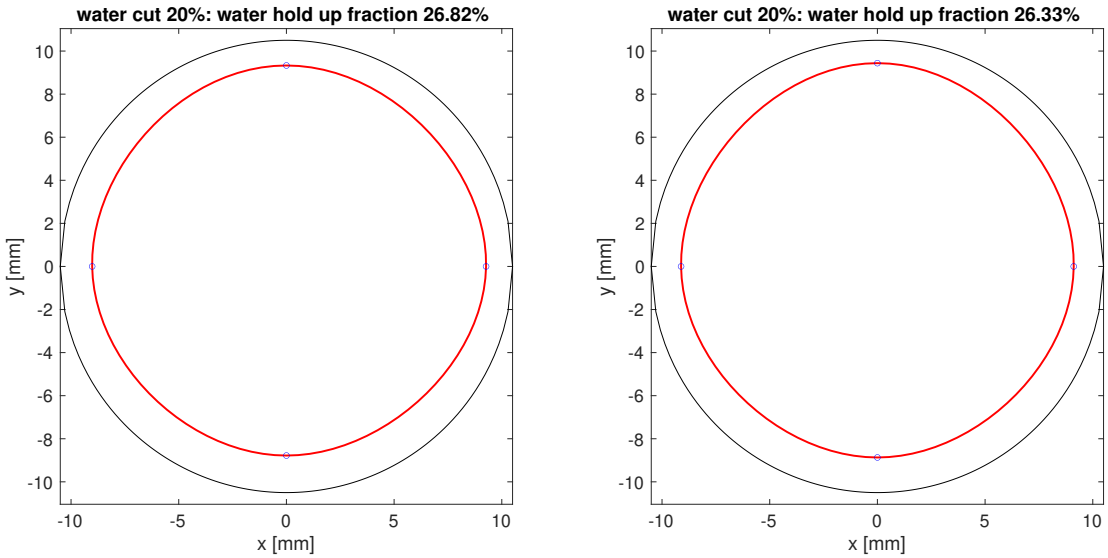

(a) Raw

(b) Processed

Figure C.6: Result of the spline function for 20% water cut and 40 °C

Bibliography

[1] Zhao An, Jin Ningde, Zhai Lusheng, and Gao Zhongke. Liquid holdup measurement in horizontal oil-water two-phase flow by using concave capacitance sensor. Meas. J. Int. Meas. Confed., 49(1):153–163, 2014. ISSN 02632241. doi: 10.1016/j.measurement.2013.11.036. URL http://dx.doi.org/10.1016/j.measurement.2013.11.036.

[2] P. Andreussi, E. Pitton, P. Ciandri, D. Picciaia, A. Vignali, M. Margarone, and A. Scozzari. Measurement of liquid film distribution in near-horizontal pipes with an array of wire probes. Flow Meas. Instrum., 47:71–82, mar 2016. ISSN 09555986. doi: 10.1016/j.flowmeasinst.2015.12.007. URL http://dx.doi.org/10.1016/j.flowmeasinst.2015.12.007https://linkinghub.elsevier.com/retrieve/pii/S0955598615300479.

[3] M.S. Arney, R. Bai, E. Guevara, D.D. Joseph, and K. Liu. Friction factor and holdup studies for lubricated pipelining–i. Int. J. Multiph. Flow, 19(6):1061–1076, 1993. ISSN 03019322. doi: 10.1016/0301-9322(93)90078-9.

[4] Barry Azzopardi and John Hills. Flow Patterns, Transitions and Models for Specific Flow Patterns. In Model. Exp. two-phase flow, pages 1–77. Springer Vienna, 2003. doi: 10.1007/978-3-7091-2538-0_1. URL http://link.springer.com/10.1007/978-3-7091-2538-0{_}1.

[5] A. C. Bannwart. Wavespeed and volumetric fraction in core annular flow. Int. J. Multiph. Flow, 24 (6):961–974, 1998. ISSN 03019322. doi: 10.1016/S0301-9322(98)00019-6.

[6] G. K. Batchelor. An Introduction to Fluid Dynamics. Cambridge University Press, feb 2000. ISBN 9780521663960. doi: 10.1017/CBO9780511800955. URL https://www.cambridge.org/core/product/identifier/9780511800955/type/book.

[7] A. Bonilla-Riano, H. F. Velasco-Pena, A. C. Bannwart, H. M. Prasser, and O. M.H. Rodriguez. Water film thickness measurement system for oil-water pipe flow. Flow Meas. Instrum., 66:86–98, 2019. ISSN 09555986. doi: 10.1016/j.flowmeasinst.2019.02.007. URL https://doi.org/10.1016/j.flowmeasinst.2019.02.007.

[8] N. Brauner. Liquid-Liquid Two-Phase Flow Systems. In Volfango Bertola, editor, Model. Exp. two-phase flow, volume 450 of CISM International Centre for Mechanical Sciences, pages 221–279. Springer Vienna, Vienna, 2003. ISBN 978-3-211-20757-4. doi: 10.1007/978-3-7091-2538-0_5. URL http://link.springer.com/10.1007/978-3-7091-2538-0{_}5.

[9] M. E. Charles, G. W. Govier, and G. W. Hodgson. The horizontal pipeline flow of equal density oil-water mixtures. Can. J. Chem. Eng., 39(1):27–36, 1961. ISSN 1939019X. doi: 10.1002/cjce.5450390106.

[10] S.W. Churchill. Friction Factor Equations Spans All Fluid-Flow Regimes. Chem. Eng. J., 84: 91–92, 1977.

[11] M. W.E. Coney. The theory and application of conductance probes for the measurement of liquid film thickness in two-phase flow. J. Phys. E., 6(9):903–910, 1973. ISSN 00223735. doi: 10.1088/0022-3735/6/9/030.

[12] Milad Darzi and Chanwoo Park. Optical distortion correction of a liquid-gas interface and contact angle in cylindrical tubes. Phys. Fluids, 29(5):052004, may 2017. ISSN 1070-6631. doi: 10.1063/1.4982902. URL http://aip.scitation.org/doi/10.1063/1.4982902.

[13] DDBST Gmbh. Surface Tension of Water. URL http://www.ddbst.com/en/EED/PCP/SFT{_}C174.php.

[14] Engineering ToolBox. Roughness & Surface Coefficients, 2003. URL https://www.engineeringtoolbox.com/surface-roughness-ventilation-ducts-d{_}209.html.

[15] Engineering ToolBox. Water - Density, Specific Weight and Thermal Expansion Coefficient, 2003. URL https://www.engineeringtoolbox.com/water-density-specific-weight-d{_}595.html.

[16] Engineering ToolBox. Water - Dynamic and Kinematic Viscosity, 2004. URL https://www.engineeringtoolbox.com/water-dynamic-kinematic-viscosity-d{_}596.html.

[17] Roberto Ibarra, Ivan Zadrazil, Omar K Matar, and Christos N Markides. Investigation of oil-water flow in horizontal pipes using simultaneous two-line planar laser- induced fluorescence and particle velocimetry SIMULTANEOUS TWO-LINE PLANAR LASER-INDUCED FLUORESCENCE AND. Number September, pages 1490–1496, 2016.

[18] IEA. Oil information: overview, 2019. URL https://www.iea.org/reports/oil-information-2019.

[19] E. M.R.M. Ingen Housz, G. Ooms, R. A.W.M. Henkes, M. J.B.M. Pourquie, A. Kidess, and R. Radhakrishnan. A comparison between numerical predictions and experimental results for horizontal core-annular flow with a turbulent annulus. Int. J. Multiph. Flow, 95:271–282, 2017. ISSN 03019322. doi: 10.1016/j.ijmultiphaseflow.2017.01.020.

[20] Eduard Ingen Housz. Experimental and numerical studies on core-annular flow through a horizontal pipe, 2016.

[21] D. D. Joseph, R. Bai, K. P. Chen, and Y. Y. Renardy. Core-annular flows. Annu. Rev. Fluid Mech., 29(1):65–90, 1997. doi: 10.1146/annurev.fluid.29.1.65.

[22] S.A. Konings. Numerical simulations of core-annular flow through a horizontal pipe. Technical report, TU Delft, 2017.

[23] J. E. Koskie, I. Mudawar, and W. G. Tiederman. Parallel-wire probes for measurement of thick liquid films. Int. J. Multiph. Flow, 15(4):521–530, 1989. ISSN 03019322. doi: 10.1016/0301-9322(89)90051-7.

[24] H. Liu. A theory of capsule lift-off in pipeline. Pipelines, 2:23–33, 1982.

[25] Rhys G. Morgan, Christos N. Markides, Ivan Zadrazil, and Geoffrey F. Hewitt. Characteristics of horizontal liquid-liquid flows in a circular pipe using simultaneous high-speed laser-induced fluorescence and particle velocimetry. Int. J. Multiph. Flow, 49:99–118, 2013. ISSN 03019322. doi: 10.1016/j.ijmultiphaseflow.2012.09.004. URL http://dx.doi.org/10.1016/j.ijmultiphaseflow.2012.09.004.

[26] G. Ooms, A. Segal, A. J. van der Wees, R. Meerhoff, and R. V.A. Oliemans. A theoretical model for core-annular flow of a very viscous oil core and a water annulus through a horizontal pipe. Int. J. Multiph. Flow, 10(1):41–60, 1983. ISSN 03019322. doi: 10.1016/0301-9322(83)90059-9.

[27] Keerthivasan Rajamani. Interfacial profiles of wavy film flow in vertical pipe at low Reynolds numbers – an experimental study. 2018.

[28] O.M.H. Rodriguez, I.H. Rodriguez, and J.L. Ansoni. An experimental and numerical study on the wall lubrication force in dispersed liquid-liquid flow. Int. J. Multiph. Flow, 120, 2019. ISSN 03019322. doi: 10.1016/j.ijmultiphaseflow.2019.103094.

[29] G. Sotgia, P. Tartarini, and E. Stalio. Experimental analysis of flow regimes and pressure drop reduction in oil-water mixtures. Int. J. Multiph. Flow, 34(12):1161–1174, 2008. ISSN 03019322. doi: 10.1016/j.ijmultiphaseflow.2008.06.001. URL http://dx.doi.org/10.1016/j.ijmultiphaseflow.2008.06.001.

[30] Domenico Strazza, Marco Demori, Vittorio Ferrari, and Pietro Poesio. Capacitance sensor for hold-up measurement in high-viscous-oil/conductive-water core-annular flows. Flow Meas. Instrum., 22(5):360–369, 2011. ISSN 09555986. doi: 10.1016/j.flowmeasinst.2011.04.008. URL http://dx.doi.org/10.1016/j.flowmeasinst.2011.04.008.

[31] A. Ullmann and N. Brauner. Closure relations for the shear stress in two-fluid models for core annular flow. 16(4):355–387, 2004.

[32] Validyne. DP15 Manual.

[33] Erik van Duin, Ruud Henkes, and Gijs Ooms. Influence of oil viscosity on oil-water core-annular flow through a horizontal pipe. Petroleum, 5(2):199–205, jun 2019. ISSN 24056561. doi: 10.1016/j.petlm.2018.01.003. URL https://linkinghub.elsevier.com/retrieve/pii/S2405656117301724.

[34] H.J. van Duin. Influence of oil viscosity on oil-water core-annular flow through a horizontal pipe, 2017.